

# UC Santa Barbara

## UC Santa Barbara Electronic Theses and Dissertations

### Title

The Interplay Between Growth and Mechanics at the Unicellular and Multicellular Levels

### Permalink

<https://escholarship.org/uc/item/8p31v81d>

### Author

Gomez, Carlos Osvaldo

### Publication Date

2023

Peer reviewed|Thesis/dissertation

UNIVERSITY OF CALIFORNIA

Santa Barbara

The Interplay Between Growth and Mechanics at the Unicellular and Multicellular Levels

A dissertation submitted in partial satisfaction of the  
requirements for the degree Doctor of Philosophy  
in Molecular, Cellular, and Developmental Biology

by

Carlos Osvaldo Gomez

Committee in charge:

Professor Otger Campàs, Co-Chair

Professor Tau-Mu Yi, Co-Chair

Professor Adele Doyle

Professor Anthony De Tomaso

Professor Kathy Foltz

June 2023

The dissertation of Carlos Osvaldo Gomez is approved.

---

Professor Adele Doyle

---

Professor Kathleen Foltz

---

Professor Anthony De Tomaso

---

Professor Tau-Mu Yi

---

Professor Otger Campàs, Committee Chairperson

June 2023

The Interplay Between Growth and Mechanics at the Unicellular and Multicellular Levels

Copyright © 2023

by

Carlos Osvaldo Gomez

To my parents, this is dedicated to you.

## ACKNOWLEDGEMENTS

I would like to begin by thanking my advisor, Otger Campàs. I am grateful for all the advice and opportunities you have given me over the course of my Ph.D. I explored many disciplines and collaborated with many people of different backgrounds. Because of this, I have become a more well-rounded scientist and learned the value of being interdisciplinary. Thank you for your patience and openness. It will not be forgotten.

I would also like to thank my co-advisor Tau-Mu Yi, and my thesis committee members, Adele Doyle, Kathleen Foltz, and Anthony De Tomaso. Thank you, Tau-Mu, for helping me at the start of my journey and providing the foundation for the rest of my Ph.D. journey.

I would like to thank all the members of the Campàs lab during my time here, Ale, Friendhelm, Adam, Elijah, James, David, Hannah, Dennis, Yucen, Jennifer, Marie, Antoine, Sangwoo, Shuo-Ting, Georgina, and Renwei. Thank you, Dennis and Yucen, for always staying and helping me with my late-night experiments and providing endless entertainment.

I would like to thank all the people from the Center for Science and Engineering Partnerships at the California NanoSystems Institute who allowed me to hone my mentorship skills and provided me with a community that made me feel at home. Thank you, Ofi, for all the support and care you provided during my time here.

I would like to thank all the people who made my graduate school experience the best it could be: Aimal, Chiamaka, Dennis, Marcela, Jin, Samhita, Yucen. Thank you, Jennie, for always being there when I needed someone. Thank you, Vanessa, for teaching me to live in the moment. And thank you, Stephanie, for making my days brighter and all the memories.

Lastly, I would like to thank my parents who have been there with me every step of the way. Thank you for everything.

VITA OF CARLOS OSVALDO GOMEZ  
May 2023

**EDUCATION**

Ph.D. in Molecular, Cellular, and Developmental Biology University of California, Santa Barbara	2023
B.S. in Bioengineering University of California, Merced	2015
B.S. in Chemical Sciences – Chemistry Emphasis University of California, Merced	2015

**PROFESSIONAL EMPLOYMENT**

Graduate Student Researcher University of California, Santa Barbara	2015 – Present
Lead Research Coordinator University of California, Santa Barbara	2018 – 2022
Teaching Assistant University of California, Santa Barbara	2015 – 2022
Research Facilitator University of Chicago – Marine Biological Laboratory	2022

**PUBLICATIONS**

Gross B, Shelton E, **Gomez C**, & Campàs O. (2021) STRESS, an automated geometrical characterization of deformable particles for *in vivo* measurements of cell and tissue mechanical stresses. bioRxiv. doi: <https://doi.org/10.1101/2021.03.26.437148>

Lim I, Vian A, van de Wouw HL, Day RA, **Gomez C**, Liu Y, Rheingold AL, Campàs O, & Sletten EM. (2020) Fluorous soluble cyanine dyes for visualizing perfluorocarbons in living systems. *Journal of American Chemical Society* 142(37): 6072-16081.

Trogdon M, Drawert B, **Gomez C**, Banavar SP, Yi T-M, Campàs O, & Petzold LR. (2018) The effect of cell geometry on polarization in budding yeast. *PLoS Computational Biology* 14(6):e1006241.

Banavar SP, **Gomez C**, Trogdon M, Petzold LR, Yi T-M, & Campàs O. (2018) Mechanical feedback coordinates cell wall expansion and assembly in yeast mating morphogenesis. *PLoS Computational Biology* 14(1):e1005940.

**Gomez C.** (2014). Regeneration of lost brain tissues by genetic manipulation of *nou-darake* in *Schmidtea mediterranea* planarias. *UC Merced Undergraduate Research Journal*, 7(1). [ucm\\_mwp\\_ucmurj\\_25002](http://escholarship.org/uc/item/3ss9j9k6). Retrieved from: <http://escholarship.org/uc/item/3ss9j9k6>

## **AWARDS**

University Award of Distinction University of California, Santa Barbara	2022
Alliance of Graduate Education and the Professoriate Fellowship National Science Foundation	2019
Science and Engineering Teaching Fellowship University of California, Santa Barbara	2018
Mellichamp Fellowship in Systems Biology and Bioengineering University of California, Santa Barbara	2017
Statewide Symposium Poster Award (Honorable Mention) National Science Foundation	2014
SACNAS Travel Scholarship Society for Advancement of Chicanos/Hispanics and Native Americans in Science	2014
AMGEN Scholar Fellowship Amgen Inc.	2014
Louis Stokes California Alliance for Minority Participation Fellowship National Science Foundation	2013

## ABSTRACT

The Interplay Between Growth and Mechanics at the Unicellular and Multicellular Levels

by

Carlos Osvaldo Gomez

Whether it is a single cell organism or a multicellular system, both need to undergo changes in mechanics in order to grow and shape themselves. In this thesis, we will look at the interplay between growth and mechanics, both at the unicellular and multicellular levels. For the single cell organism, we will look at how the mechanics of the cell wall are maintained during the process of tip growth in *S. cerevisiae* and explore the interplay of cell wall assembly and mechanics during the process of mating projection growth. For the multicellular system, we will characterize how the forces change during the process of growth and invasion in 4T1 breast cancer spheroids.

Single celled organisms have various forms of growth, but a common type is called tip growth. In yeast, this mode of growth occurs during mating whereby two cells of different mating types grow towards each other. While the molecular pathways of this process have been documented, it is unclear how the mechanical integrity of the cell wall is maintained under the high internal turgor pressure of the organism during cell wall assembly and expansion. By combining theoretical and experimental approaches, we show that mechanical feedback is necessary to allow mating projection growth to occur in *S.*

*cerevisiae*. We found that the mechanical feedback is provided by the Cell Wall Integrity pathway, which modulates cell wall assembly depending on mechanical changes in the cell wall and stabilizes mating projection growth. By experimentally perturbing key players of this pathway through genetic deletions of cell wall stress sensors, we were able to test the predictions provided by our theoretical description. Our results show that cell wall assembly and the mechanics of the cell wall must be tightly coordinated via a genetically-encoded mechanical feedback to ensure cell viability during morphogenesis.

Multicellular cancer aggregates have been used as model systems to study different aspects of tumorigenesis. Here we will investigate the mechanical aspects of the process of invasion, which is one of the initial steps of metastatic growth. Multicellular aggregates, also called spheroids, have been used extensively as they are more representative of the physiology of a tumor and can be embedded in controlled microenvironments. While the forces that a tumor generates on the surrounding environment have been investigated, the forces within the tumor during invasion have never been explored, mainly due to a lack in technologies enabling direct mechanical measurements in 3D multicellular environments. By utilizing fluorescent cell-sized bioinert droplets as force transducers, we quantify how the mechanics within the tumor change as it begins to invade into a collagen type I matrix. Through the use of this technique and in-house developed software, we were able to show that while supracellular stresses remain low and constant during invasion, cell-scale stresses increase in invading spheroids while stresses in the non-invading spheroids stay relatively constant.

## TABLE OF CONTENTS

I. Introduction .....	1
A. Role of Mechanics in Biological Processes .....	1
B. Unicellular System: <i>S. cerevisiae</i> .....	2
1. Process of Pheromone-Induced Growth .....	3
2. Basis of Theoretical Model for Pheromone-Induced Growth .....	3
C. Multicellular System: 4T1 Murine Breast Cancer Spheroid.....	4
1. Initial Process of Metastatic Growth .....	5
2. Using Microdroplets to Quantify Forces in 3D .....	5
D. Outline .....	6
II. Unicellular System: Mating Projection Growth in <i>S. cerevisiae</i> .....	8
A. Introduction.....	8
B. Theoretical Description.....	13
1. Cell Wall Mechanics and Extension.....	14
2. Dynamics of Cell Wall Assembly .....	15
C. Stability of Mating Projection Growth.....	20
D. Characteristics of Stably Growing Mating Projection .....	23
E. Discussion .....	28
F. Methods .....	32
III. Multicellular System: Initial Stages of Metastatic Growth in 4T1 Spheroids.....	35
A. Introduction.....	36
B. Characterization of Model Tumor Invasion.....	38

C. Endogenous Mechanical Stresses in Non-Invading and Invading Model	
Tumors .....	42
D. Supracellular Stresses are Low and Constant in Both Invading and Non-Invading Spheroids.....	45
E. Cell-Scale Stresses are Different in Invading and Non-Invading	
Tumors .....	48
F. Discussion.....	50
G. Methods .....	54
IV. Conclusions .....	59
References.....	62
Appendix.....	73

## **I. Introduction**

How mechanics influence biological processes has been a question of interest that spans decades [1, 2, 3]. It has been shown through various studies that mechanical cues are important in the development [4, 5] and shaping of biological systems [6, 7], but the exact link is difficult to find. This can be attributed to various factors such as molecular redundancy [8, 9] or technological limitation [10, 11]. In order to gain a greater understanding of the role of mechanics in biology, I have collaborated with graduate students from various backgrounds to determine this link through modelling and direct measurements. The goal of this thesis is to further our current understanding of the interplay between growth and mechanics from the unicellular and multicellular perspectives. For this reason, this document has been divided into two sections, the first section focuses on how mechanical feedback is required for proper growth and polarization in the unicellular organism *S. cerevisiae* and the second section focuses on how the mechanical properties of multicellular tumor spheroids change upon invasion. With these studies, we aimed to demonstrate how mechanics play a role in the biological processes of growth.

### ***A. Role of Mechanics in Biological Processes***

The process by which living organisms change their shape and form is called morphogenesis. This process occurs in all living organisms and is run, in part, by genetic processes encoded in each. Whether it is single-celled or multicellular, the way organisms develop is also bound by the laws of physics [12]. One example that best exemplifies this concept can be found in early *Drosophila* embryos. By simply compressing the embryo during development, it was found that Twist expression, which is required for the

ventralization of the embryo, can be induced showing that changes in mechanics, in this case growth, can influence genetic expression as it is required for proper development of the organism [13]. How these genetic processes coordinate within the physical constraints of our world are still not fully understood, but many approaches have been used to gain a better understanding. In our work with budding yeast, we utilize theoretical modeling to understand how the cell wall maintains its integrity during expansion and growth. In our work with *in vitro* tumors, we utilize a microdroplet technique to directly measure how the physical properties change as it begins to invade into its microenvironment. While two vastly different approaches were used, they both helped further our understanding the interplay between mechanics and growth.

### ***B. Unicellular System: S. cerevisiae***

The role of mechanics at the unicellular level has been observed in a wide variety of biological processes ranging from cell fate decisions to motility [14, 15], but how are mechanical cues processed to control cellular shape? To begin, we must understand how cellular shape is determined. The shape of an individual cell is primarily determined by either the actomyosin cortex in animal cells [16] or by the cell wall in walled cells [17]. To gain further insight into how mechanics influence biochemical determinants of cellular shape and vice versa, we have chosen to study this interplay in the unicellular eukaryote *S. cerevisiae* for the mechanical forces and signaling components guiding morphogenesis are better understood than in higher eukaryotes.

## 1. Process of Pheromone-Induced Growth

Budding yeast has three modes of growth: budding, pheromone-induced, and filamentous. While each mode of growth could be assessed for our purposes, we have chosen to investigate pheromone-induced growth as it is more controllable than budding, which is regulated by the cell cycle, and better characterized than filamentous growth, which cross-talks with other important signaling pathways [18].

Pheromone-induced growth begins with exposure to a mating pheromone from the opposite mating type (i.e. a- or  $\alpha$ -factor for mating type  $\alpha$  or a respectively). This pheromone is detected by its specific receptor leading to the activation of a heterotrimeric G-protein causing its  $G\alpha$  and  $G\beta\gamma$  subunits to dissociate and diffuse throughout the membrane. Dissociation of the  $G\beta\gamma$  subunit allows for the recruitment of Cdc24 which activates the small G-protein Cdc42, the master regulator of cell polarization. The presence and activation of Cdc42 then furthers the recruitment of proteins responsible for polarized growth to the plasma membrane. This cluster of proteins has been termed the polarisome [19]. Within this structure resides a protein called Bni1, the only formin in *S. cerevisiae* found to play a role in pheromone-induced growth, and once activated, it nucleates actin cables [20]. This allows secretory vesicles containing proteins and enzymes responsible for degrading and rebuilding the wall to be localized to a specific region. This balance of degradation and assembly in addition to the presence of a high internal turgor pressure allows the cell to grow a mating projection.

## 2. Basis for Theoretical Model of Pheromone-Induced Growth

For budding yeast to undergo pheromone-induced growth, there must be an expansion of the cell wall. The cell wall, which is composed of glycans and chitin, is only about 100 nm

wide, but its strong interwoven network provides enough strength to keep the cell from bursting [21]. Upon local degradation of the cell wall caused by the breaking of these glycan chains, there is a change in its viscosity allowing this region to expand under high turgor pressure. This expansion is counterbalanced by the deposition of new wall material brought in by secretory vesicles, which were alerted of the stress on the wall by several cell wall stress sensors (Wsc1, Wsc2, Wsc3, Mid2, and Mtl1) that propagated the signal to Rho1, the master regulator of cell wall integrity, and its downstream effector Fks1/2, glucan synthases responsible for adding new material to the wall. Previous published values for physical properties of the wall and activation rates of key CWI components were used to build upon previous work that combined cell wall mechanics and growth in tip growing cells [22] resulting in a model for how the cell interprets the mechanical state of the wall and responds to these changes.

### ***C. Multicellular System: 4T1 Murine Breast Cancer Spheroid***

As one can imagine, the complexity and scale of multicellular systems can range immensely [23]. For that reason, we wanted to use a system that would increase the complexity but would not overcomplicate it. We utilized multicellular aggregates that were composed of one cell type and decided on 4T1 murine breast cancer cells as preliminary studies revealed that they make aggregates without the aid of any additional components. These aggregated cells have been used to understand a variety of processes including metastasis, which is the spread of cancer cells to distal regions of the organism.

## 1. Initial Process of Metastatic Growth

Cancer is one of the leading causes of death worldwide [24]. As such, much research has focused on how to treat it. From understanding where the most common mutations occur [25,26] to developing chemotherapeutics to stop its progression [27,28], it was found that the process of metastasis, where cells spread from a primary tumor to distal regions of the body, is actually responsible for 60-90% of cancer related deaths [29,30]. The process of metastasis for solid tumors begins as all cancers do, by mutations to oncogenes [31]. Once the oncogene has been mutated, the primary tumor begins to form. After this, local invasion into the basement membrane begins by degradation and reorganization of its surrounding microenvironment [32]. This is followed by the process of intravasation where the cells enter the bloodstream and then seed to a distal region where they begin the process of making a secondary tumor [33]. This process occurs at the system level of the organism and has many variables associated to it. Therefore, we wanted to investigate one of the initial steps, invasion, and understand if the forces within the actual tumor change during this process. The process of invasion utilizes a variety of enzymes to degrade the basement membrane, but for simplicity, we chose to make the microenvironment solely of one of its main components: collagen type I [34]. The reason for this is due to the variability of commercially available matrices, which could affect the mechanics of the system [35]. By using only one component, we can eliminate one variable in our experimental setup and still observe the process of invasion.

## 2. Using Microdroplets to Quantify Forces in 3D

Many techniques have been developed to measure the mechanical forces generated by individual cells [36], but only a few can measure the mechanical stresses of tissues,

especially in 3D [37]. For this reason, obtaining measurements of mechanical forces of 3D cell culture systems has proven difficult. A novel technique which utilizes fluorescent hydrogel beads has been able to obtain measurements of the mechanical stresses in 3D cell culture systems, but due to their composition, the cells seem to crawl over the hydrogel bead [38]. Additionally, their results demonstrated an odd phenomenon which showed strong actin activity around the hydrogel, which could have occurred due to the cells being able to attach and crawl on the bead. To circumvent these and other technical issues, we opted to utilize oil droplets, the first technique established to measure mechanical stresses in 3D multicellular systems [39, 40]. This technique utilizes an oil that is bioinert, whose interfacial tension is controlled by commercially available surfactants, and contains a far-red fluorophore to allow imaging of said oil. The oil is then injected into the tissue of choice to act as a force transducer to measure the anisotropic stresses of the system. This technique has been demonstrated to work in biological systems [39, 40] and was developed to further our understanding of how mechanics play a role in biology.

#### ***D. Outline***

The purpose of this work was to gain a better understanding of how the mechanics change during two different morphogenic events at different scales. While at different scales, we find that the interplay of mechanics and growth plays a pivotal role in their processes.

In chapter 2, we discuss how the shaping of tip walled cells requires coordination of cell mechanics and growth. Using the model organism, *S. cerevisiae*, we show that mechanical feedback is necessary to enable this communication of the mechanical state of the cell wall to the genetic processes maintaining it, allowing the coordination of cell wall expansion and

growth. My part in this work was performing experimental perturbations that could provide support for the theoretical framework developed and its results. Through the contributions that I made, we were able to show phenotypes that were representative of the theoretical predictions made, that mechanical feedback was necessary not only for proper development of the mating projection, but also its shape.

In chapter 3, we discuss how the forces within *in vitro* tumors change during invasion. Using 4T1 spheroids, we show that the stresses within an *in vitro* tumor increase over the course of invasion by the use of oil microdroplets. The process of invasion involves the degradation and rearrangement of the surroundings while the individual cells from the tumor push and pull into this reorganized space. Because of this, our hypothesis was that the droplet would experience higher forces as the process continues. My part in this work was collecting the data and quantifying the results through software that was made in-house. Through my contributions, we were able to show that the stresses of the interior of the tumor increase as the tumor cells invade the surrounding area.

We conclude in Chapter 4 by summarizing our results and discussing future directions.

## **II. Unicellular System: Mating Projection Growth in *S. cerevisiae***

From cell division to polarization and growth, cells constantly change their shapes to perform specific tasks [41–43]. These morphological changes are achieved through remodeling of the structures that mechanically sustain the cell, such as the cytoskeleton in animal cells and the cell wall in walled cells. Unlike animal cells, which can undergo fast and complex cell shape changes, walled cells must take extra care during shape changes, as the cell wall needs to mechanically sustain their high internal turgor pressure throughout the cell wall remodeling process [44–46]. A lack of coordination between cell wall expansion and assembly during cell growth can be fatal for the cell, as the thinning of the cell wall in expanding regions may lead to cell lysis unless it is carefully balanced by newly assembled wall material. While it is believed that the coordination of cell wall expansion and assembly is necessary to cell wall remodeling and morphogenesis, the mechanisms behind this coordination remain largely unknown. This work was done in collaboration with Samhita Banavar, who designed the theoretical framework, and Michael Trogdon, who aided in the computational analysis. I was responsible for performing the wet-lab experiments. Otger Campàs, Tau-Mu Yi, and Linda Petzold provided supervision over our respective contributions. This chapter was published in *PLoS Computational Biology* [47].

### ***A. Introduction***

Cell shape changes are ultimately governed by the mechanical state of the cell wall [45, 46, 48]. Studies of the mechanics of walled cell morphogenesis have predominantly focused on tip-growing cells of plant and fungal species because of their large size, simpler geometry and fast growth rates [49–51]. In this highly polarized growth mode, cells adopt a tubular

shape that extends only at the apical region (Fig. 1). During this process, cells polarize their cytoskeleton and localize exocytosis to the growing region, exactly where the cell wall needs to be assembled and remodeled. While the molecular underpinnings of tip-growth differ across species, two basic features have been shown to be necessary [49]: polarized assembly of new cell wall material at the tip, and nonhomogeneous mechanical properties enabling its apical expansion (Fig. 1F). Previous theoretical descriptions of tip-growth focused on cell wall assembly [52-54] or cell wall mechanics [51, 54, 56] separately. More recent descriptions accounted for both cell wall assembly and mechanics [57-60], but assumed these processes to be independent of each other. As we show below by directly solving the dynamics of cell wall assembly and expansion, assuming cell wall mechanics and assembly to be independent of each other always leads to unstable cell wall expansion and cell lysis, in stark contrast with experimental observations. Despite its relevance to cell viability during cell wall remodeling and morphogenesis, no previous theoretical descriptions have addressed the role of coordination (coupling or feedback) between cell wall mechanics and assembly in the morphogenesis of walled cells.

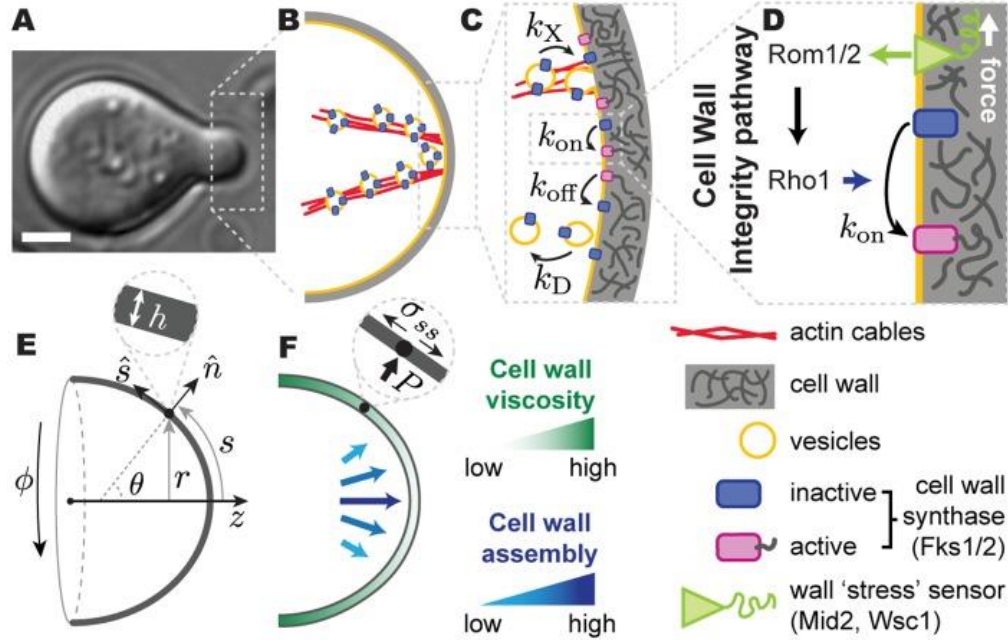


**Figure 1. Schematic diagrams of relevant events and quantities in mating projection growth.** (A) Transmitted light image of a *S. cerevisiae* cell growing a mating projection in the presence of  $\alpha$ -factor. Scale bar,  $2\mu\text{m}$ . (B-D) Sketch of molecular events leading to the delivery and activation of cell wall synthases Fks1/2 at the apex. See main text and Table 1 for definitions of parameters. (E) Geometry of the system and definition of the relevant variables. (F) Sketch depicting the increasing cell wall viscosity and decreasing cell wall assembly away from the apex. The inset depicts local normal force balance at the cell wall. All variables are defined in the main text.

In addition to well-known model systems for tip-growth, such as pollen tubes in plants and hyphal growth in higher fungi [48-50], budding yeast display tip-growth during mating. Haploid cells secrete pheromone ( $\alpha$ - and a-factors for mating types a and  $\alpha$ , respectively) that elicits the growth a tubular mating projection from the partner of the opposite type [61 - 62] (Fig. 1A). Since the molecular basis of cell polarization and cell wall assembly and remodeling have been extensively studied in budding yeast, tip-growth of mating projections provide a unique system to study the mechanism of coordination between cell wall mechanics and assembly.

In a-cells, binding of  $\alpha$ -factor to its cognate receptor activates the heterotrimeric G-protein, leading to the activation and polarization of the small G-protein Cdc42, a master regulator of cell polarization [63]. Cdc42-mediated polarization recruits various molecular factors to an apical region of the plasma membrane known as the polarisome, where the formin protein Bni1 drives the nucleation of actin cables, focusing exocytosis at the apex [43, 61] (Fig. 1B). Secretory vesicles transporting Fks1/2 cell wall synthases and cell wall remodeling enzymes (e.g., glucanases) move along actin cables to the exocyst, eventually leading to the incorporation of Fks1/2 synthases to the plasma membrane and the release of glucanases into the preexisting cell wall (Fig. 1B and 1C) [64-67]. Together, these events molecularly and mechanically polarize the cell, causing a localized expansion of the cell wall at the apex (Fig. 1B and 1F).

In general, the expansion of the cell wall is a vulnerable situation that must be carefully controlled. Since the cell wall sustains the high internal turgor pressure, uncontrolled cell wall expansion can lead to cell wall piercing and cell lysis. In budding yeast, the Cell Wall Integrity (CWI) pathway is known to help the cell prevent loss of cell wall mechanical integrity in a variety of situations [68-71], from mating pheromone-induced growth to vegetative growth [69, 70, 72]. Five transmembrane proteins, namely Wsc1, Wsc2, Wsc3, Mid2, and Mtl1, are thought to act as stress sensors and relay information about the mechanical state of the cell wall to multiple intracellular processes via the activation of Rho1 GTPases [69, 70, 72-78]. Previous works have shown that Wsc1 and, especially, Mid2 play an important role during mating pheromone induced growth, while the remaining stress sensors do not seem to strongly affect projection growth [78-82]. While the specific mechanical quantity that these stress sensors monitor in the cell wall remains unclear,

activation of the CWI pathway leads to the downstream Rho1-mediated activation of several key molecular components, including cell wall synthases (Fks1/2), actin nucleators (Bni1) and mediators of exocytosis (Sec3), and also induces a transcriptional response via a MAPK cascade [70]. The activation of cell wall Fks1/2 synthases [62, 70, 74] provides the most direct coupling between cell wall mechanics and assembly and could potentially stabilize mating projection growth (Fig. 1D). However, it is unknown if such a simple, direct mechanical feedback can stabilize morphogenesis of walled cells by itself.

Using mating projection growth in budding yeast as a model system, and combining experiments and theory, we show that coordination between cell wall mechanics and assembly through direct Fks1/2 activation in the CWI pathway (mechanical feedback) stabilizes mating projection growth without affecting its geometry. In what follows, the term ‘mechanical feedback’ refers to the nature of the input signal that is sensed and relayed by stress sensors in the CWI pathway. We first derive a theoretical description that connects the cell wall mechanics to the intracellular processes building the wall (Fks1/2 activation dynamics) via the CWI pathway, and show that stable projection growth can only persist in the presence of mechanical feedback. In the absence of coordination between cell wall assembly and mechanics, cell wall expansion is always unstable, leading to either progressive thickening or thinning of the cell wall depending on conditions. Our experimental results indicate the compromising the mechanical feedback through genetic deletions of the wall stress sensors Mid2 and Wsc1, and also through perturbations of cell wall mechanics and increased turgor pressure, all lead to defects in mating projection growth and cell viability. Our experimental observations are in agreement with the theoretical predictions, suggesting that the mechanical feedback provided by the CWI pathway via

direct activation of Fks1/2 synthases can stabilize projection growth without altering cell geometry. In addition, by directly measuring the size of the exocytosis region in wild-type (WT) and mutants with compromised mechanical feedback, we show that the size of the mating projection is controlled by the size of the exocytosis region, but is independent of the strength of the mechanical feedback, as predicted theoretically. Altogether, our results show that a mechanical feedback between cell wall mechanics and assembly is essential for stability of cell wall expansion and projection growth, but that its geometry and size are insensitive to the mechanical feedback.

### ***B. Theoretical Description***

The expansion of the cell wall during morphogenesis is powered by the cell's internal turgor pressure,  $P$ . Such high pressure is mechanically sustained by the cell wall, which provides mechanical integrity to the cell at all stages, including during mating projection growth. Similarly to other organisms [45, 48, 50], the cell wall in budding yeast can be considered a thin shell surrounding the cell, as the wall thickness ( $\sim 100$  nm [85]) is much smaller than the radius of the projection ( $\sim 1\mu\text{m}$  [86]). Since the cell's shape is determined by the location of its cell wall, we describe the growth of the mating projection as the expansion of an axisymmetric thin shell, parametrized by the arclength  $s$  from the projection apex and azimuthal angle  $\phi$  (Fig. 1E). The shape of the projection is characterized by its local radius,  $r(s, t)$ , and the principal curvatures  $\kappa_s = \partial\theta/\partial s$  and  $\kappa_\phi = \sin\theta/r$ , respectively, where  $\theta(s, t)$  is the angle between the local outward normal and the axis of growth (Fig 1E). The coordinates  $(r, \phi, z)$  (Fig. 1E) are standard cylindrical coordinates, and the angle  $\theta$  and arclength  $s$  parameterize changes in normal and tangential directions of the

surface,  $\hat{n}$  and  $\hat{s}$  respectively [60, 87] (Fig. 1E). The time evolution of the mating projection shape is governed by the mechanics and assembly of the cell wall, as described below.

### 1. Cell Wall Mechanics and Extension

Building on previous work combining cell wall mechanics and growth in tip-growing cells [60], as well as on the expansion of thin viscous shells [87], we write the equations governing the dynamics of the growing cell wall. Local normal force balance at the cell wall reads

$$\sigma_{ss}\kappa_s + \sigma_{\phi\phi}\kappa_\phi = P \quad \text{and} \quad \sigma_{ss}\kappa_\phi = \frac{P}{2} \quad (1)$$

where  $\sigma_{ss}(s, t)$  and  $\sigma_{\phi\phi}(s, t)$  are the tensions along  $s$  and  $\phi$  in the wall (Fig 1F). The expansion of the cell wall during growth is caused by the tensions and depends on the mechanical properties (rheology) of the cell wall, which govern the response of the cell wall to applied stresses. Although the yeast cell wall behaves elastically at short time scales (seconds [85]), it expands irreversibly on the characteristic timescales of mating projection growth (minutes [57]), revealing a fluid-like behavior of the cell wall in growing regions. The transition between fluid-like behavior at the growing apical region to an elastic behavior far away from the apex has been studied in other systems and it is believed to be controlled by an increasing concentration of cross-links between wall polymers away from the tip [88, 89]. This is consistent with the higher concentration of cell wall degrading enzymes (glucanases) in the apical region of the mating projection [90]. We therefore assume the cell wall of the growing mating projection to behave as an inhomogeneous viscous fluid, with spatially varying viscosity  $\mu(s)$ , minimal at the apex and increasing away from it (Fig. 1F). The local tangential velocity  $u(s, t)$  of a cell wall with constant density  $\rho_w$ , or its strain

(expansion) rates  $\dot{\epsilon}_s = \partial u / \partial s$  and  $\dot{\epsilon}_\phi = (1/r)(dr/dt)$  equivalently, can be minimally related to the tensions in the wall by [60, 87]

$$\sigma_{ss} = 4\mu h[\dot{\epsilon}_s + \frac{\dot{\epsilon}_\phi}{2}] \quad \text{and} \quad \sigma_{\phi\phi} = 4\mu h[\frac{\dot{\epsilon}_s}{2} + \dot{\epsilon}_\phi] \quad (2)$$

## 2. Dynamics of Cell Wall Assembly

Sustained expansion of the cell wall during mating projection growth requires constant assembly of new cell wall material in the expanding apical region (Fig. 1B, 1C and 1F). Cell wall assembly occurs through synthesis of the primary component of the wall, 1,3- $\beta$  glucan [85], by transmembrane 1,3- $\beta$  glucan synthases Fks1/2, which localize at the apical, growing region of the mating projection [91-92]. While only inactive Fks1/2 molecules, unable to synthesize glucans, are incorporated to the plasma membrane through exocytosis, Fks1/2 can be activated by Rho1 once at the plasma membrane [93] (Fig. 1C and 1D). The activated form of Fks1/2 synthases extrudes 1,3- $\beta$  glucan chains into the extracellular space, thereby assembling new cell wall onto the preexisting wall [44]. Accounting for these events, mass conservation of cell wall material yields

$$\partial_t(rh) + \partial_s(rhu) = \frac{rm_m k_p}{\rho_w} \rho_A(s, t) \quad (3)$$

where  $h(s, t)$  is the cell wall thickness (Fig. 1E), and  $m_m$  and  $k_p$  are the mass of a 1,3- $\beta$  glucan monomer and the 1,3- $\beta$  glucan assembly rate by Fks1/2 synthases, respectively. For simplicity, we assume that the assembly rate of new cell wall material is proportional to the local surface density  $\rho_A$  of active Fks1/2. Given that Fks1/2 synthases are constantly added and removed from the plasma membrane by exo- and endo-cytosis, it is important to consider their dynamics.

Inactive Fks1/2 are transported to the apical region of the mating projection by the cell's exocytic machinery and incorporated to the plasma membrane via exocytosis [94] (Fig. 1C). Once on the membrane, inactive Fks1/2 molecules, characterized by a local density  $\rho_I$ , can be activated at a rate  $k_{on}$ . Due to the relatively fast exo- and endocytosis Fks1/2 recycling ( $\sim 1$ s [95]) and very low diffusion constant  $D$  of proteins on yeast membranes ( $D \sim 0.01 \mu\text{m}^2/\text{s}$  [96]), the diffusive movement of inactive Fks1/2 on the plasma membrane can be neglected. In the active state, Fks1/2 extrudes new 1,3- $\beta$  glucan chains into the wall, which get assembled into the preexisting 1,3- $\beta$  glucan network, effectively attaching active Fks1/2 to the wall and leading to a wall-driven convective movement of active Fks1/2 with velocity  $u$ . Finally, active Fks1/2 synthases become inactive at a rate  $k_{off}$  (Fig. 1C). The dynamics for both inactive and active Fks1/2 states can be written in the curved geometry of the cell as

$$\begin{aligned} [\partial_t(p_I r) &= r[k_{off}\rho_A - k_{on}\rho_I] + r[k_X\rho_0 - k_D\rho_I], \\ \partial_t(\rho_A r) + \partial_s(\rho_A r u) &= r[k_{on}\rho_I - k_{off}\rho_A] \end{aligned} \quad (4)$$

where  $k_X$  and  $k_D$  are the exocytosis and endocytosis rates, respectively. Experimental observations of the spatial distribution of both exocytic and endocytic events during mating projection growth indicate that these are maximal at the apex and decay away from it [95]. These localized exo- and endo-cytosis profiles are characterized by a decay length scale and can be written as  $k_X(s, t) = k_X^0 \exp(-s^2/\lambda_X^2)$  and  $k_D(s, t) = k_D^0 \exp(-s^2/\lambda_D^2)$ , where  $k_X^0$  and  $k_D^0$  are the apical rates of exocytosis and endocytosis, respectively, and  $\lambda_X$  and  $\lambda_D$  are the length scales over which exocytosis and endocytosis decay, respectively. Given that the enzymes that locally degrade the cell wall and control its mechanical properties are secreted through exocytosis [97], we assume the length scale of viscosity variation to be set by the exocytosis length scale and write the viscosity profile as  $\mu(s) = \mu_0 \exp(s^2/\lambda_X^2)$ .

In order to simultaneously solve for the mechanics of cell wall expansion and the dynamics of cell wall assembly described above, it is necessary to specify the activation and inactivation rates of membrane-localized Fks1/2 cell wall synthases,  $k_{on}$  and  $k_{off}$ , respectively. Inactivation of active, membrane-localized Fks1/2 synthases has been largely unexplored and assumed here to occur at a constant rate. The activation of inactive Fks1/2 is mediated by the GTPase Rho1 through the CWI pathway [62, 70, 74] (Fig. 1D), providing a direct coupling between the local mechanical state of the wall and the local cell wall synthesis machinery via the Fks1/2 activation rate  $k_{on}$  (Fig. 1D). To account for this coupling, we write the Fks1/2 activation rate  $k_{on}$  as dependent on the cell wall mechanical state, namely

$$k_{on} = \Gamma[\dot{\epsilon}_s + \dot{\epsilon}_\phi] \quad (5)$$

where we assumed the stress sensors to perceive the expansion (strain) rate in the wall, rather than strain or stress. Indeed, activation of cell wall synthases should not occur in the absence of cell wall expansion, as it could otherwise lead to uncontrolled cell wall thickening. Eq. 5 constitutes a direct mechanical feedback of cell wall mechanics on cell wall assembly, with the dimensionless parameter  $\Gamma$  establishing the strength of the mechanical feedback: large values of  $\Gamma$  indicate that low levels of cell wall expansion trigger large activation of Fks1/2 synthases, and vice versa.

Combining Eqs. 1–5 and the profiles of exocytosis, endocytosis and wall viscosity described above, we solve the coupled dynamics of cell wall mechanical expansion and assembly. Normalizing all variables, we find 5 dimensionless parameters that control the dynamical regimes of the system (Table 1), namely  $k_{off}/k_X^0$ ,  $k_D^0/k_X^0$ ,  $\lambda_D/\lambda_X$ ,  $\Gamma$ , and the ratio

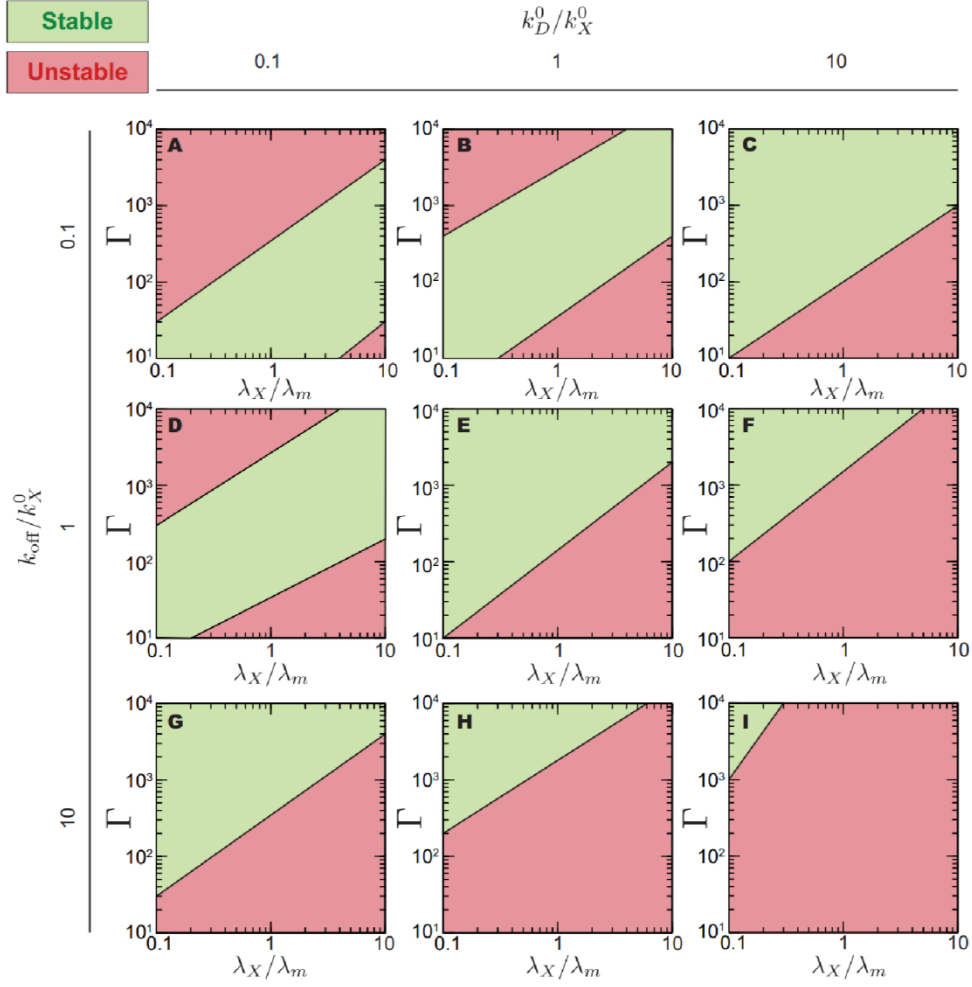


**Figure 2. Dynamical regimes.** Parameter space spanned by  $\Gamma$  and  $\lambda_X/\lambda_m$  (A-I) for different values of the parameters  $k_D^0/k_X^0$  and  $k_{off}/k_X^0$ . The transition from unstable growth (red) to stable growth (green) exists in all cases.

$(P\rho_w\lambda_X)/(12\mu_0m_w\rho_0k_p)$ , which corresponds to the ratio  $\lambda_X/\lambda_m$  of the exocytosis length scale  $\lambda_X$  and a length scale  $\lambda_m \equiv 12\mu_0m_w\rho_0k_p/P\rho_w$  set by the expansion mechanics of the cell wall.

The parameters  $k_{off}/k_X^0$ ,  $k_D^0/k_X^0$ ,  $\lambda_D/\lambda_X$  have either been measured or estimated and we use below their known values [95, 98] (Table A in Appendix); variations in these parameters

do not qualitatively affect our results. We vary the parameters held constant in the main text within a reasonable range and determine the dynamical regimes. Since our theoretical predictions and experimental results indicate that the instability occur as the pressure is increased or the mechanical feedback decreased, we explore if this behavior is robust as we vary all other parameters. Varying the parameters  $k_D^0/k_X^0$  and  $k_{off}/k_X^0$  by two orders of magnitude (from 0.10 to 10) does not change our qualitative results (Fig. 2): there is transition between stable and unstable states, and the critical value of the mechanical feedback strength increases with  $\lambda_X/\lambda_m$ . Varying  $\lambda_X/\lambda_D$  leads also to the same qualitative results.

Dimensionless Parameters				
$\frac{P\rho_w\lambda_X}{12\mu_0m_w\rho_0k_p}$	$\Gamma$	$\frac{k_{off}}{k_X^0}$	$\frac{k_D^0}{k_X^0}$	$\frac{\lambda_D}{\lambda_X}$
Physical/Chemical Parameters				
$P$	Turgor pressure of budding yeast	$\lambda_X$	Exocytosis length-scale	
$\rho_w$	Density of 1,3- $\beta$ glucans in cell wall	$\lambda_D$	Endocytosis length-scale	
$\mu_0$	Apical viscosity of cell wall	$k_X^0$	Apical rate of exocytosis	
$m_w$	Mass of 1,3- $\beta$ glucan monomer	$k_{off}$	Inactivation rate of Fks1/2	
$\rho_0$	Density of Fks1/2 enzymes in vesicle			
$k_p$	Extrusion rate of 1,3- $\beta$ glucan monomer			

**Table 1.** System physical parameters and relevant dimensionless parameters.

### *C. Stability of Mating Projection Growth*

In the absence of mechanical feedback ( $\Gamma = 0$ ), the equation 2.4 cannot lead to mating projection growth is unstable for any value of the parameters. We find that in the absence of mechanical feedback the cell wall either progressively thins, eventually leading to either cell wall piercing, or thickens, leading to unbounded cell wall growth, depending on parameter values. This instability arises from the lack of coordination between cell wall expansion and assembly: changes in cell wall expansion cannot be balanced by cell wall assembly unless the processes building the cell wall have information about how cell wall expansion is changing on the cell's surface.

In the presence of mechanical feedback ( $\Gamma > 0$ ), numerical integration of Eqs. 1–5 (Methods) shows that stable states of mating projection growth can be sustained for a large range of parameters (Fig 3F and 3). In this context, stable states refer to sustained steady state growth of the mating projection at constant velocity. For any given value of the ratio  $(P\rho_w\lambda_x)/(12\mu_0m_w\rho_0k_p)$  there exists a critical value of the feedback strength  $\Gamma$  below which mating projection growth is unstable. Similarly, for every value of the feedback strength  $\Gamma$ , there is a maximal value of  $(P\rho_w\lambda_x)/(12\mu_0m_w\rho_0k_p)$  above which mating projection growth becomes unstable. This instability is caused by the progressive thinning of the apical cell wall, eventually causing the piercing of the cell and leading to cell lysis. The bifurcation between stable and unstable states characterizes the transition between stably growing mating projections and a situation in which this stable growth cannot be sustained because of the progressive thinning of the cell wall and its eventual piercing. This instability

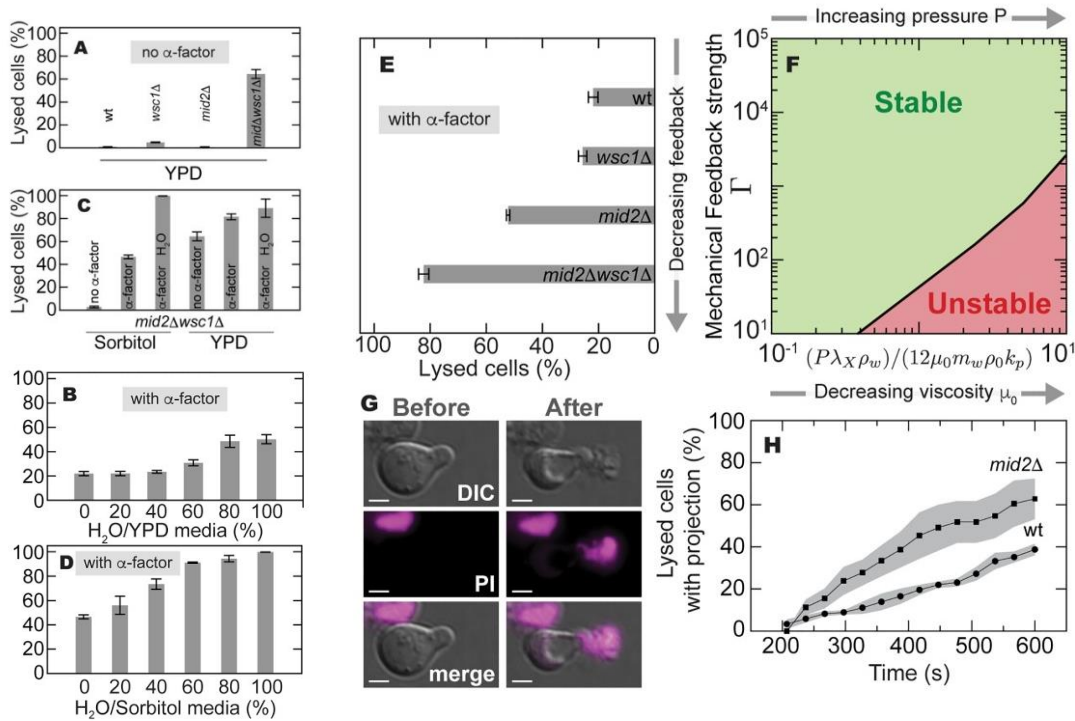


**Figure 3. Effect of mechanical feedback strength and turgor pressure on cell viability.** The strength of mechanical feedback,  $\Gamma$ , is experimentally varied by deleting *MID2* and *WSC1*. The dimensionless parameter  $(P\rho_w\lambda_X)/(12\mu_0m_w\rho_0k_p)$  is varied by changing the osmolarity of the external medium through dilution of the yeast growth media, YPD, in deionized H<sub>2</sub>O, effectively increasing turgor pressure  $P$  in cells. Cell lysis was measured using the PI staining viability assay (Methods). (A) Percent of lysed cells in the absence of  $\alpha$ -factor for WT, *mid2* $\Delta$  and *wsc1* $\Delta$  mutants, as well as the *mid2* $\Delta$ *wsc1* $\Delta$  double mutant. (B) Percent of WT lysed cells when grown in the presence of  $\alpha$ -factor in YPD medium with decreasing osmolarity. (C) Percent of *mid2* $\Delta$  *wsc1* $\Delta$  lysed cells when grown both in the presence and absence of  $\alpha$ -factor in YPD, in osmotically supported conditions (YPD + 1M sorbitol), as well as in hypo-osmotic conditions (100% H<sub>2</sub>O). (D) Percent of *mid2* $\Delta$  *wsc1* $\Delta$  lysed cells when grown in the presence of  $\alpha$ -factor and osmotically supported media (YPD + sorbitol), diluted for decreasing osmolarities. (E) Percent of lysed cells in *mid2* $\Delta$  and *wsc1* $\Delta$  mutants, as well as the *mid2* $\Delta$ *wsc1* $\Delta$  double mutant, when grown in the presence of  $\alpha$ -factor in YPD. (F) Theoretically predicted dynamical regimes for varying values of the mechanical feedback strength  $\Gamma$  and the ratio  $(P\rho_w\lambda_X)/(12\mu_0m_w\rho_0k_p)$ . Decreasing osmolarity experimentally, corresponds to increasing  $P$  and, therefore, moving along horizontal lines in the positive direction. Addition of zymolyase, a cell wall degrading enzyme, corresponds to decreasing the cell wall viscosity, moving also along horizontal lines in the positive direction. (G) Images (DIC, PI staining and merge) showing the moments before and after the piercing of the cell wall at the tip of a mating projection and subsequent cell lysis of a *mid2* $\Delta$  cell after the addition of zymolyase. Scale bar, 2 $\mu$ m. (H) Temporal increase in the fraction of pierced mating projections for both *mid2* $\Delta$  (squares) and WT (circles) cells after addition of zymolyase.

minimal viscosity), above (below) which the cell wall progressively thins and eventually pierces at the tip of the projection, leading to cell lysis. The predicted increase of the maximal turgor pressure or decrease in the minimal wall viscosity for increasing feedback strength  $\Gamma$  indicates that cells with compromised mechanical feedback should be more sensitive to both an increase in turgor pressure or a decrease in wall viscosity than WT cells.

In order to experimentally explore the predicted dynamical regimes (Fig. 3F and Fig. 2), we systematically varied the mechanical feedback strength, as well as the turgor pressure  $P$  and cell wall viscosity  $\mu_0$ . In contrast to previous works, here we examine all three perturbations in the context of the stability of pheromone-induced projection growth. We first varied the feedback strength  $\Gamma$  by compromising the ability of the cell to sense the mechanical state of the wall. To this end, we genetically deleted the two primary cell wall stress sensors present during mating projection growth, namely Wsc1 and Mid2 [74] (Fig. 1D), and measured the resulting cell lysis (Methods). Only in the presence of  $\alpha$ -factor and mating projection growth, did the deletion of either of the two sensors (Mid2, Wsc1) lead to increased levels of cell lysis compared to WT (Fig. 3A and 3E), as predicted theoretically (Fig 3F), indicating that the ability to sense the mechanical state of the wall is essential during growth. Moreover, the double mutant *mid2 $\Delta$ wsc1 $\Delta$*  exhibited the highest level of cell lysis in  $\alpha$ -factor and, even when osmotically supported by 1M sorbitol, showed a substantial increase in lysis after the addition of  $\alpha$ -factor (Fig. 3A, 3C and 3E). These observations show that the double mutant has an enhanced sensitivity to the addition of mating pheromone, in agreement with previous results obtained during vegetative growth [81]. To explore how changes in the parameter  $(P\rho_w\lambda_x)/(12\mu_0m_w\rho_0k_p)$  affected cell viability (Fig. 3F), we independently changed the turgor pressure  $P$  and the cell wall viscosity  $\mu_0$ . To

increase the cell's turgor pressure  $P$ , we progressively decreased the osmolarity of the external medium (Methods). We observed a monotonic increase in lysed cells for both WT and *mid2Δwsc1Δ* cells as media osmolarity was decreased in the presence of  $\alpha$ -factor (Fig. 3B and 3D), consistent with the theoretically predicted effect of increased turgor pressure  $P$  (Fig. 3F). Finally, in order to decrease the cell wall viscosity  $\mu_0$ , thereby increasing the value of the parameter  $(P\rho_w\lambda_x)/(12\mu_0m_w\rho_0k_p)$  (Fig. 3F), we added zymolyase to the culture media (Methods). Zymolyase enzymatic activity degrades 1,3- $\beta$  glucans in the cell wall, effectively lowering the cell wall viscosity. Addition of zymolyase led to the piercing of the cell wall typically at the tip of the mating projection (Fig. 3G), as expected theoretically (Fig. 3F). Since zymolyase will continuously degrade the cell wall, leading to the eventual piercing and lysis of all cells, we studied the temporal increase in pierced cells. Our results indicate that *mid2Δ* cells with reduced mechanical feedback pierced faster than WT cells when grown at the same zymolyase concentration (Fig. 3H), as theoretically expected (Fig. 3F). Overall, our experimental results are in agreement with our theoretical predictions (Fig. 3F) and are consistent with the CWI pathway providing the necessary mechanical feedback to coordinate cell wall expansion and assembly.

#### ***D. Characteristics of Stably Growing Mating Projections***

Stable, steady-state solutions for mating projection growth show that the shape of the mating projection is largely insensitive to variations in the feedback strength  $\Gamma$  and the ratio  $(P\rho_w\lambda_x)/(12\mu_0m_w\rho_0k_p)$  (Fig. 4A, 4B, 4E and 4F). The size (radius)  $R$  of the mating projection increases linearly with the size of the exocytosis region  $\lambda_x$ , but it is independent from the feedback strength  $\Gamma$  (Fig. 4B). Beyond projection shape and size, the cell wall expansion rate,  $\dot{\epsilon}_s + \dot{\epsilon}_\phi$ , is always maximal at the projection apex ( $s = 0$ ) and decreases

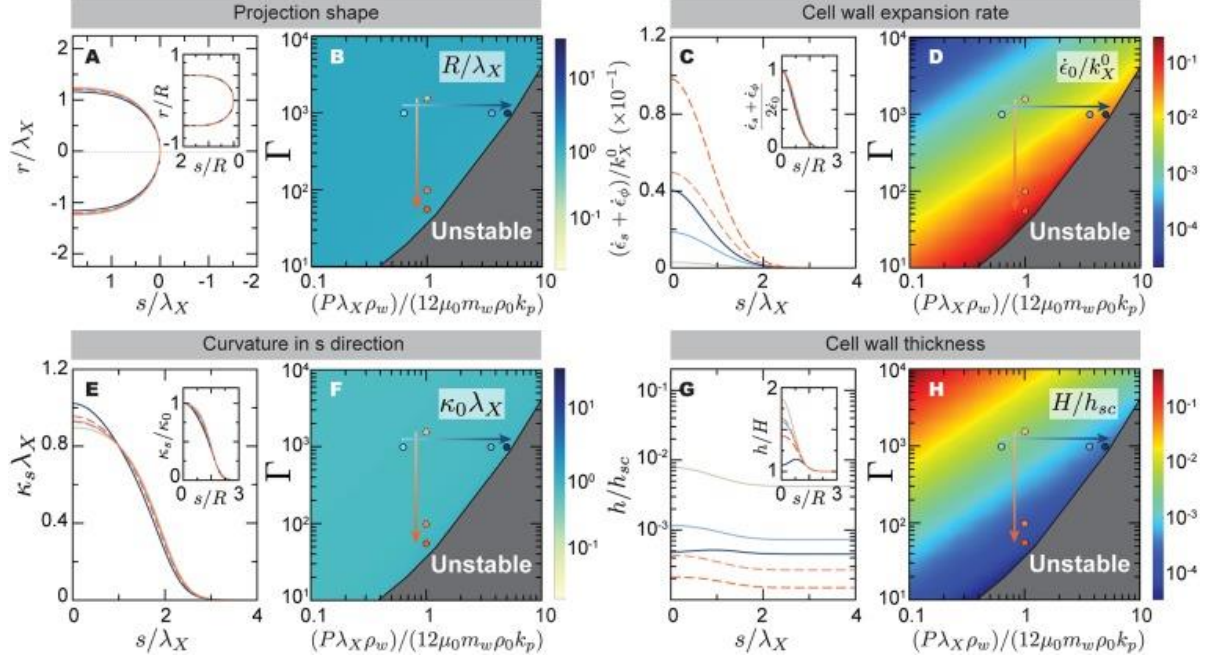


**Figure 4. Steady-state stable solutions for mating projection growth: Projection shape and cell wall expansion.** (A,C,E,G) Mating projection shape (A), as well as the spatial profiles of the cell wall expansion rate  $\dot{\epsilon}_s + \dot{\epsilon}_\phi$  (C), curvature  $\kappa_s$  (E) and cell wall thickness  $h$  (G), for different values of the mechanical feedback strength  $\Gamma$  and the ratio  $\lambda_X/\lambda_m = (P\rho_w\lambda_X)/(12\mu_0m_w\rho_0k_p)$ . All insets show a different scaling of each magnitude, with the arclength normalized by the projection radius  $R$  and each quantity normalized by its value at the projection tip ( $s = 0$ ), with the exception of the wall thickness  $h(s)$  and the shape  $r(s)$ , which are normalized by the limiting values far away from the apical region,  $H$  and  $R$  respectively. The color code indicates the different parameter values, shown as dots of the same color in the parameter space right to each panel. Increasing orange and blue tones of the dots corresponds to decreasing  $\Gamma$  and increasing  $(P\rho_w\lambda_X)/(12\mu_0m_w\rho_0k_p)$ , respectively (arrows in Fig 2E). (B,D,F,H) The variation of the apical value of each magnitude, namely  $\dot{\epsilon}_0 \equiv \dot{\epsilon}_s(s=0) = \dot{\epsilon}_\phi(s=0)$  (D) and  $\kappa_0 \equiv \kappa_s(s=0)$  (F), is shown for the different values of the parameters for which stable states exist. The variation of the projection radius and wall thickness away from the apical region,  $R$  (B) and  $H$  (H) respectively, are shown as a function of the parameters as well.

away from it (Fig 4C), eventually vanishing as no wall expansion occurs far away from the growing apical region. The cell wall expansion rate at the projection apex,  $(\dot{\epsilon}_s + \dot{\epsilon}_\phi)|_{s=0}$ , increases with increasing turgor pressure (or  $(P\rho_w\lambda_X)/(12\mu_0m_w\rho_0k_p)$  equivalently) and with decreasing mechanical feedback strength (Fig. 4C and 4D). In contrast, the apical cell wall thickness displays the opposite behavior (Fig. 4G and 4H), decreasing for increasing  $P$

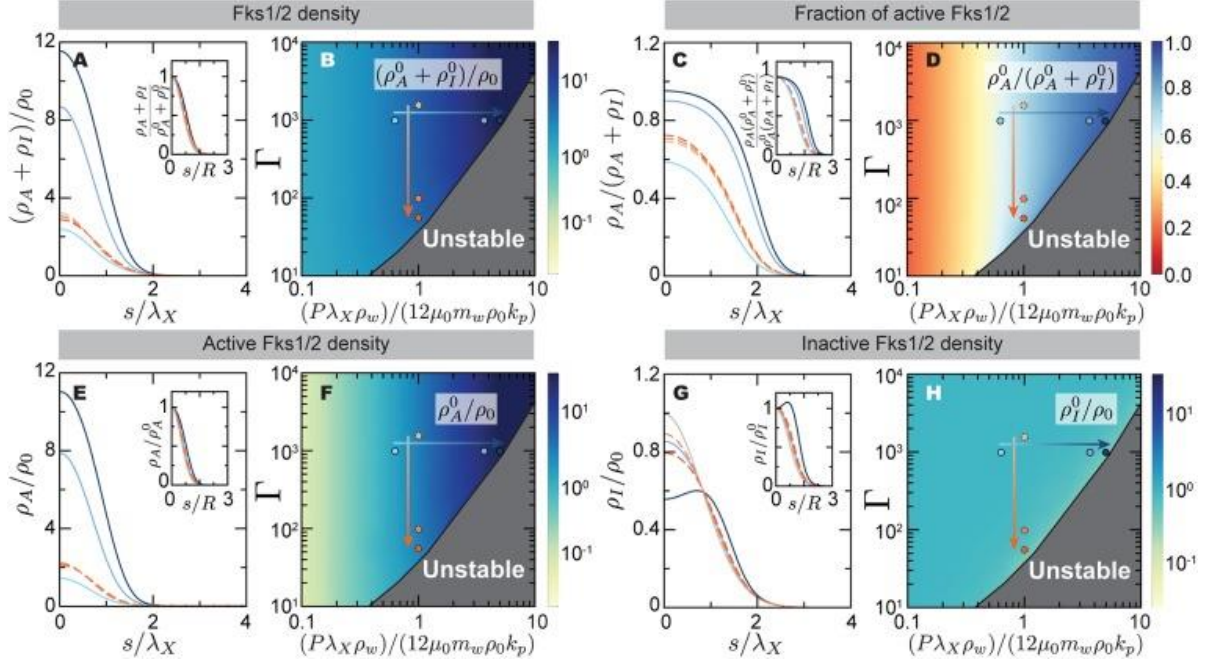


**Figure 5. Steady-state stable solutions for mating projection growth: Cell wall assembly via Fks1/2.** Cell wall assembly via Fks1/2. (A,C,E,G) Total Fks1/2 density  $\rho_A + \rho_I$  (A), fraction of active Fks1/2,  $\rho_A/(\rho_A + \rho_I)$  (C), active Fks1/2 density (E) and inactive Fks1/2 density (E), for different values of the mechanical feedback strength  $\Gamma$  and the ratio  $\lambda_X/\lambda_m = (P\rho_w\lambda_X)/(12\mu_0 m_w \rho_0 k_p)$ . All insets show a different scaling of each magnitude, with the arclength normalized by the projection radius  $R$  and each quantity normalized by its value at the projection tip ( $s = 0$ ). The color code indicates the different parameter values, shown as dots of the same color in the parameter space right to each panel. Increasing orange and blue tones of the dots corresponds to decreasing  $\Gamma$  and increasing  $(P\rho_w\lambda_X)/(12\mu_0 m_w \rho_0 k_p)$ , respectively (arrows in Fig 2E). (B,D,F,H) The variation of the apical value of each magnitude, namely  $(\rho_A^0 + \rho_I^0)/\rho_0$  (B),  $\rho_A^0/(\rho_A^0 + \rho_I^0)$  (D),  $\rho_A^0/\rho_0$ (F) and  $\rho_I^0/\rho_0$ (H), is shown for the different values of the parameters for which stable states exist.

or decreasing  $\Gamma$ . These results indicate that cells closer to the instability threshold display stronger apical cell wall expansion rates and thinner cell wall (Figs. 3E, 4D, and 4H), suggesting the strong cell wall expansion and thinning at the apex as the cause of the loss in cell wall mechanical stability.

Regarding cell wall assembly during stable, steady-state projection growth, our theoretical results indicate maximal cell wall assembly at the expanding apical region. Both the total surface density of Fks1/2 synthases,  $\rho_A + \rho_I$ , and the surface density of only active

Fks1/2 synthases,  $\rho_A$ , are maximal at the apex and decrease away from it until they vanish (Fig. 5A, 5B, 5E and 5F), as expected from the apically-localized exo- and endo-cytosis profiles. The apical value of the total (or only active) Fks1/2 surface density, namely  $\rho_A^0 + \rho_I^0$  (or  $\rho_A^0$ ), can be either smaller or larger than the surface density  $\rho_0$  of Fks1/2 synthases secreted by exocytic vesicles (Fig. 5A, 5B, 5E and 5F). The reason why the total Fks1/2 surface density  $\rho_A^0 + \rho_I^0$  can be larger than  $\rho_0$  at the apex is that active Fks1/2 is secreting 1,3- $\beta$  glucans into the cell wall, a process that effectively anchors them to the wall, holding secreted Fks1/2 synthases to the tip region and increasing its concentration there. Beyond Fks1/2, anchoring transmembrane proteins to the cell wall can potentially be used as a mechanism to locally increase the protein concentration on the membrane to levels well-beyond secretion levels. The fraction of active Fks1/2,  $\rho_A/(\rho_A + \rho_I)$ , is also maximal at the apex and decreases away from it (Fig. 5C and 5D). This is because of mechanical feedback, which induces more Fks1/2 activation at the apex following the larger cell wall expansion rate in this region (Fig. 4C). Finally, the surface concentration of inactive Fks1/2 also decreases away from the expanding tip because of tip-localized exo- and endo-cytosis (Fig. 5G and 5H). Non-monotonic profiles of inactive Fks1/2 occur because high cell wall expansion rates at the tip lead to more Fks1/2 activation, leaving less inactive Fks1/2 molecules in this region. Altogether, these results indicate that at the instability threshold, the apical cell wall expansion rate becomes too large to be balanced by cell wall assembly, leading to the progressive thinning of the cell wall and cell lysis.

The theoretical results above predict that both the geometry and size of the growing mating projection are independent from the mechanical feedback strength  $\Gamma$ , and that the projection radius increases with the size of the exocytosis region (Figs. 6A and 6B and 4A

and 4B). To experimentally explore how exocytosis and the mechanical feedback strength affect the mating projection size  $R$  (Fig 6A), we employed a deletion mutant for *Spa2*, a scaffold protein that localizes Bni1 and is recruited by Cdc42 [64], which displays a very wide mating projection compared to WT (Fig 6C and 6D). We visualized the exocytosis region in both WT and *spa2Δ* cells by expressing GFP-tagged Sec3, a component of the exocyst that marks exocytic sites [43]. The exocytosis length scale  $\lambda_X$  (Fig. 6A), which we measured directly from confocal images (Fig. 6C and 6D and Methods), is considerably larger in *spa2Δ* mutant cells than in WT cells (Fig. 6E), indicating that a larger mating projection radius  $R$  is associated with a larger size of the exocytosis region. In contrast, the size  $R$  of the mating projection was not observed to vary with changes in the strength of the

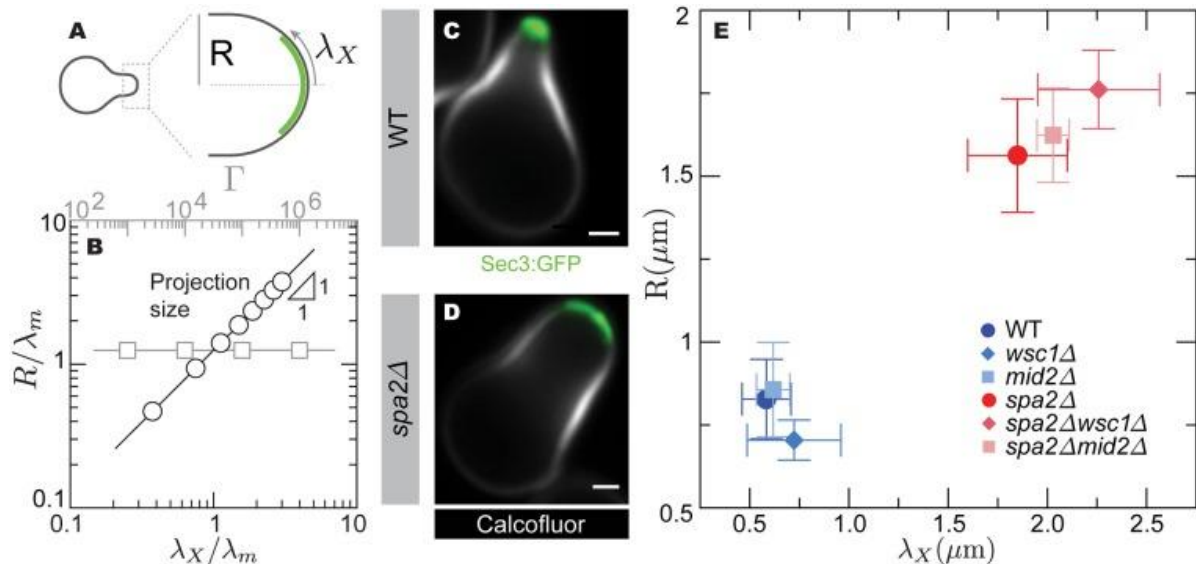


**Figure 6. Control of mating projection size.** (A) Diagram of a growing mating projection showing the mating projection radius  $R$  and length scale of the secretion region (green),  $\lambda_X$ . (B) Theoretically predicted dependence of the projection radius  $R$  with the length scale of the secretion region,  $\lambda_X$ , and the strength of mechanical feedback,  $\Gamma$ . (C-D) Confocal images of WT (C) and *spa2Δ* (D) mutant cells growing mating projections. The cell wall is labeled with calcofluor (white) and the exocytosis profile is defined by Sec3-GFP (green). Scale bar, 1  $\mu\text{m}$ . (E) Measured average cell radius,  $R$ , and exocytosis length scale,  $\lambda_X$ , for *mid2Δ* and *wsc1Δ* mutants in both WT and *spa2Δ* backgrounds (*mid2Δ*,  $N = 6$ ; *wsc1Δ*,  $N = 9$ ; *spa2Δ mid2Δ*,  $N = 7$ ; *spa2Δ wsc1Δ*,  $N = 6$ ), as well as for WT ( $N = 7$ ) and *spa2Δ* ( $N = 6$ ) cells. Mean and standard deviation are shown.

mechanical feedback  $\Gamma$  (Fig. 6E), as shown by deleting *Mid2* or *Wsc1* in both WT and *spa2 $\Delta$*  backgrounds, while simultaneously measuring the size of the mating projection  $R$  and the length of the exocytosis region using *Sec3-GFP*. While deletion of *Wsc1* and *Mid2* strongly affects mating projection stability (Fig. 3E), our measurements show that it does not affect the size of the mating projection (Fig. 6E). These results indicate that the mechanical feedback is essential to sustain stable mating projection growth, but it does not affect mating projection size, which is controlled by the exocytosis profile, as predicted theoretically (Fig. 6B).

### ***E. Discussion***

In this work, we studied both theoretically and experimentally how the mechanics of cell wall expansion and the molecular processes assembling the cell wall are coordinated during cell morphogenesis, using budding yeast mating projection growth as a model system. We first derived a theoretical description of mating projection growth that couples, through mechanical feedback encoded in the CWI pathway, the cell wall expansion and geometry to the molecular processes building the cell wall. The theoretical predictions were tested experimentally through genetic deletions affecting the feedback strength and also through mechanical perturbations (hyposmotic shocks and cell wall degradation). Our theoretical predictions are in good agreement with the experimental results and indicate that the existence of mechanical feedback is essential to guarantee stability during cell wall remodeling and cell morphogenesis.

This theoretical description of mating projection growth connects the mechanics of the cell wall to the molecular events in charge of sensing its mechanical state and controlling its assembly via well-established signaling pathways (CWI pathway), thus providing specific

predictions on how mutations can affect cell morphogenesis. Several previous models accounted for both the mechanics and assembly (remodeling) of the cell wall [57-60], as we have done above, but did not account for a connection to known molecular feedback control (CWI pathway) coupling wall mechanics and assembly. These models consider the cell wall to be either a elastic material undergoing remodeling [58-59] or an elastoplastic material [57], as opposed to our description of the cell wall as a viscous fluid, which has also been considered before [60]. Importantly, at long timescales over which cell growth and cell wall remodeling occur, assuming the cell wall to be a viscous fluid, a remodeled elastic material or an elastoplastic material is largely equivalent because all of them properly account for the observed irreversible expansion (flow) of the cell wall at long timescales [57]. While previous descriptions assumed that irreversible cell wall expansion only occurs when new cell wall material is inserted into the pre-existing wall [58-59], we allowed the possibility of cell wall expansion even in the absence of cell wall assembly because the cell wall can be fluidized by the action of wall degrading enzymes secreted via exocytosis. Indeed, addition of zymolyase leads to cell wall piercing for cells with intact cell wall assembly (Fig. 3G). Such cell wall degrading enzymes are known to play an important role in cell wall remodeling [70, 100] and the establishment of inhomogeneous cell wall material properties in several organisms [88, 101], including budding yeast [57]. Since these enzymes are secreted via exocytosis, we assumed the length scale of viscosity variation away from the apex to be the same as the exocytosis region. Finally, the combination of the observed inhomogeneous stiffness of the cell wall during mating projection growth [57] (measured at short timescales; seconds) and cell wall remodeling can be theoretically described as an

effective inhomogeneous viscosity at timescales longer than cell wall remodeling, as we assumed in our description above and also done previously for other systems [60].

In the absence of any mechanical feedback relaying information about the mechanical state of the cell wall to the intracellular processes building it, our theoretical data indicate that cell wall expansion is unstable, leading to cell lysis. Previous works have shown that the cell wall is prone to piercing in cell if the CWI is compromised [70], and our experimental data indicates that degradation of the cell wall by zymolyase (effectively lowering the cell wall viscosity in our description) also leads to cell wall piercing (Fig. 3G). Since cell wall piercing involves changes in cell wall thickness, our theoretical description accounts for the dynamics of cell wall thickness from first principles (mass conservation). This is in contrast to previous models that also consider cell wall mechanics and assembly, which assume the cell wall thickness to be constant, fixed by an unknown mechanism [57-59]. Considering a variable cell wall thickness was done before [60], but the cell wall mechanics and assembly were considered independently (no mechanical feedback) and the dynamics of cell growth was not studied. We theoretically show that accounting for the simplest mechanical feedback encoded in the CWI pathway, which directly couples cell wall expansion and assembly via direct activation of Fks1/2 synthases, stabilizes cell wall expansion for a wide range of parameters. The agreement between our theoretical predictions and experimental results suggests that the specific mechanical feedback studied herein, with cell wall stress sensors Wsc1 and Mid2 locally sensing cell wall expansion and directly activating Fks1/2 cell wall synthases, can stabilize cell wall remodeling during mating projection growth by itself. Such mechanical feedback ensures that in regions where the cell wall expands the fastest (at the projection apex) and could potentially rupture via thinning, local activation of

cell wall synthases increases assembly of cell wall material, preventing cell wall rupture and stabilizing mating projection growth. However, our work does not rule out that other mechanical feedbacks encoded in the CWI pathway could also play a role in the stabilization of projection growth. It also is likely that other stress sensors [69-70], expressed during different cell wall remodeling events in budding yeast, coordinate cell wall expansion and assembly in other morphogenetic processes. While our experimental observations qualitatively agree with our theoretical predictions regarding the existence of an instability associated to the thinning of the cell wall and then need of mechanical feedback to coordinate cell wall extension and assembly, further experiments will be needed to fully confirm this scenario.

Beyond budding yeast, many other organisms, including other fungi, plants and bacteria, have walled cells that are constantly remodeled [45, 50, 102, 103]. The molecular control of cell wall remodeling and morphogenesis differs across species, and it is therefore likely that different mechanisms encode mechanical feedback in other species. Indeed, previous observations have hinted at the existence of mechanical feedback [104], but the feedback mechanisms remain elusive. The mechanical feedback described herein, or different feedback mechanisms to be discovered, may also play an important role in the coordination of cell polarity and morphogenesis in both animal and walled cells [104-107].

While essential to ensuring stability during cell wall expansion, our results show that the strength of mechanical feedback does not affect mating projection shape or size (Figs. 4 and 6) The observed decoupling in the control of cell geometry and growth stability reported here may allow cells to maintain a functional shape under different growth conditions. In addition, we find that projection size is controlled by the spatial extent of exocytosis. This is

in agreement with recent observations in fission yeast indicating that the size of the apical growth domain correlates best with the size of the apical exocytosis region [58], and also with theoretical models of fission yeast that predict the radius of the cell to be determined by the size of the apical cell wall assembly region [59].

More generally, the need to coordinate growth processes and mechanics during morphogenesis is important for individual cells, but also for tissues and organs. Identifying the molecular mechanisms enabling this coordination at different scales and in different organisms will substantially contribute to our understanding of morphogenetic processes.

## ***F. Methods***

### **Numerical integration of governing equations.**

The system of Eqs. 1–5 was scaled and written in a manner such that  $r$ ,  $h$ ,  $\rho_A$ , and  $\rho_I$  were described by equations evolving in time, and  $u$ ,  $\theta$ ,  $\kappa_s$  by differential equations in  $s$ . The latter equations were solved by the method of lines;  $s$  was discretized and the  $s$ -derivatives were written as a differential matrix using fourth order central difference and one sided finite differences at the boundary. The resulting system becomes a differential algebraic system (DAE), which was solved using Sundials, a suite of nonlinear and DAE solvers. Steady state solutions were obtained by ensuring that all time derivatives of scaled variables were below  $10^{-3}$ .

### **Yeast strains and culture conditions.**

All yeast strains were derivatives of W303-1A and contained the *bar1Δ* mutation that prevents  $\alpha$ -factor degradation by deletion of the Bar1 protease. Genetic techniques were performed per standard methods [31]. Yeast strains used in this study are listed in Table B in Appendix. All strains were cultured in YPD (yeast extract-peptone-dextrose) media

supplemented with adenine. The *wsc1Δmid2Δ* strain was grown in YPD media with 1M sorbitol to increase viability. Gene deletions and GFP-tagging were constructed by genomic integration using vectors amplified and targeted by PCR primers [32].

#### **Cell viability measurements.**

Cell lysis was determined by propidium iodide (Molecular Probes) staining. Propidium iodide (PI) was prepared in DMSO at a concentration of 20 mM and then diluted 1:1000 for use. Propidium iodide was added to cells after being exposed to  $\alpha$ -factor (1  $\mu$ M) for 2 hours. To observe the viability of cells after altering the osmotic pressure, we diluted the YPD media with distilled water upon addition of propidium iodide. The cells were imaged on slides after being exposed to propidium iodide for 10 minutes. Brightfield and fluorescent (RFP filter set) images were acquired using an inverted Nikon Eclipse TE300 microscope with a 60x objective (NA = 1.4). Image analysis was manually performed using ImageJ. Data from 3 samples for each condition was averaged and, for each sample, 150 cells or more were analyzed.

#### **Cell lysis due to zymolyase.**

To decrease the viscosity of the cell wall, we utilized zymolyase, which contains  $\beta$ -1,3 glucanase, to hydrolyze the glucan linkages that strengthen the wall. Zymolyase (Zymo Research, 1  $\mu$ l (2 units) per 100  $\mu$ l of cells) was added to cells exposed to alpha-factor for 1.5 hours. Cells were treated additionally with concanavalin A to immobilize them during the imaging process. The cells were imaged on slides for 7 minutes after being exposed to zymolyase for 3 minutes. DIC images were acquired every 3 seconds. Data from 5 samples for each condition was averaged and, for each sample, 15 cells or more were analyzed. Image analysis was manually performed using ImageJ.

### **Imaging and analyzing exocytosis.**

The length-scale of exocytosis was measured in strains that contained Sec3 fused to GFP. Calcofluor White Stain (Sigma-Aldrich) was added to cells 10 minutes prior to imaging (final concentration 0.1mg/ml) to distinguish the cell wall during image analysis. To properly visualize the length-scale and reduce imaging noise, we averaged 30 consecutive confocal images, taken at 2 second time intervals, for each cell, after incubation in 1  $\mu$ M  $\alpha$ -factor for 1 hour and 30 minutes. For *spa2 $\Delta$*  cells, the 30 images were taken at 13 second intervals to average over a longer time period to average out the stronger fluctuations in polarization in this mutant. Images were acquired with a laser-scanning confocal microscope (Zeiss LSM 710), using a 100x objective (NA = 1.4). The cells were immobilized to a glass-bottom dish coated with concanavalin A. To horizontally orient the mating projections, we layered a YPD (supplemented with 1  $\mu$ M  $\alpha$ -factor) agarose pad on top of the cells. Image analysis was manually performed using ImageJ.

### III. Multicellular System: Initial Stages of Metastatic Growth in 4T1

#### Spheroids

Metastasis, the spreading of malignant cells from a primary solid tumor, is a key event in cancer progression and ultimately one of the major causes of patient death. The spreading of tumor cells requires the invasion of cells into surrounding tissues, a physical process likely linked to mechanical changes in tumors. While the mechanics of the tumor microenvironment is known to play an important role in tumor progression, the endogenous mechanical stresses inside tumors, and their changes during invasion, remain largely unknown. Combining new image analysis methods and direct mechanical stress measurements of model *in vitro* tumors (spheroids) of 4T1 murine breast cancer cells, here we show that invading and non-invading tumors display differences in their mechanical behavior. While supracellular stresses are low (100 Pa) and remain constant in both invading and their non-invading counterparts, cellular stresses inside invading tumors increase consistently during invasion, with non-invading tumors displaying the opposite behavior. Moreover, cellular stresses display increasing variability during tumor invasion, with peak values well over 1000 Pa, as opposed to non-invading tumors, for which cell stress variability decreases over time. These results indicate that changes in internal tumor mechanics may play an important role in their ability to invade surrounding tissues. This work was done in collaboration with Johannes Soltwedel who developed the image analysis software. I was responsible for performing the experiments. This chapter is currently being prepared for submission.

## ***A. Introduction***

Cancer is one of the leading causes of death worldwide [24]. The molecular diversity among patients and the complexity of tumor progression in different tissues [108, 109] have hindered efforts towards successful treatment. Most previous studies have focused on the role of molecular cues, genetic mutations, cell behavior, interaction among different cell types and changes in the tumor microenvironment [110, 111]. These studies and many others have shown that after the onset of the disease, eventual death is due to the spread of the tumor to multiple organs from an original, individual and localized tumor. Beyond specific molecular changes, the spreading of malignant cells from the original tumor requires the physical invasion of tumor cells into their immediate surrounding tissue. Despite the many molecular studies of this process, the mechanical stresses in isolated tumors and the mechanical changes inside the tumor that occur during its invasion of their surroundings are still unclear.

Mechanics is known to play a key role in many developmental processes, from tissue morphogenesis to collective cell migration, as well as in cancer progression [113, 114, 115]. *In vitro* studies have shown that the material properties of the tumor microenvironment change the ability of tumors to invade [116, 117, 118]. For instance, a malignant transformation of non-malignant MCF10A cells can be induced by increasing the stiffness of the microenvironment [119]. Also, many studies have shown that cancer cells are softer than their healthy counterparts, with their invasive potential correlating with their stiffness [120, 121], a phenomena thought to help invading tumor cells pass through small openings in the tissue (intravasation). Using traction force microscopy, it has been possible to quantify the forces of invading tumor cells on synthetic 3D substrates and while the stiffness of the

cell has been correlated with higher invasion potential, it was found that non-malignant cells can also apply high forces on the environment, but that high force is not the only component necessary for invasion to occur [122]. While each of these studies provides novel information about mechanical changes for individual cells and their environment, the cellular forces within 3D tumors during invasion have not been quantified, mainly due to the technical challenges associated with measuring mechanical stresses in 3D multicellular systems.

Microdroplet techniques have been recently developed to perform *in situ* measurements of cell and tissue mechanical stresses in living 3D tissues [123, 124]. In addition to multiple applications *in vivo* and *ex vivo*, microdroplets have also been used to quantify the contributions of tensile and compressive stresses in growing multicellular spheroids *in vitro*<sup>19</sup>. Gel beads were later developed as microdroplet alternatives that allow the additional quantification of tissue pressure and tangential stresses, and have been also used to measure mechanical stresses in spheroids *in vitro* [126, 127, 128]. While these techniques have revealed some of the mechanical forces generated by cells in multicellular systems, the mechanical stresses at play within isolated tumors and their changes during tumor invasion remain unknown.

To reveal the mechanical stresses in model tumors, we used oil microdroplets and compared the mechanical stresses in invading and non-invading tumors. To focus on the mechanical changes during invasion while minimizing the complexity of the system, we generated spheroids of highly invasive 4T1 murine breast cancer cells and embedded them in different hydrogel matrices to control the invasion process. In particular, we quantified both cell-scale and supracellular stresses in spheroids of 4T1 murine breast cancer cells

embedded in agarose (non-invading) and in a type I collagen matrix (invading), which mimics physiologically relevant microenvironments. Using a new image analysis pipeline, we analyzed the characteristics of invading model tumors while simultaneously measuring the endogenous mechanical stresses in them. By comparing the results in invading type I collagen-embedded tumors and non-invading agarose-embedded tumors, we reveal the changes in endogenous mechanical stresses that occur specifically during invasion.

### ***B. Characterization of model tumor invasion***

To reveal the mechanical differences between invading tumor spheroids and their non-invading counterparts, we first generated spheroids of fluorescently-labelled (cytoplasmic marker) 4T1 murine breast cancer cells using the hanging droplet technique (Fig. 1a; Methods). Once the spheroids were compact (after 3 days), we injected a single, fluorescently-labelled oil microdroplet in each one of them to monitor the mechanical stresses inside the spheroid (Fig. 1b; Methods). Droplet-injected spheroids were then embedded in either an agarose or a collagen I matrix. Previously used techniques to embed spheroids in hydrogel matrices were unsuccessful with droplet-injected spheroids due to the additional weight of the droplet, which caused the spheroids to completely sink in the chamber before matrix rigidification [129]. To overcome this, we developed a new mounting system consisting of a dual hydrogel cylindrical chamber that enables the control of spheroid positioning during hydrogel rigidification (Methods). The spheroid was first embedded into the desired hydrogel in a cylindrical chamber, which was later further embedded into a larger cylindrical agarose chamber to provide better structural integrity to the system. With this method, it was possible to embed droplet-injected spheroids in either agarose or collagen I and image them for long time periods, as the cylindrical geometry of

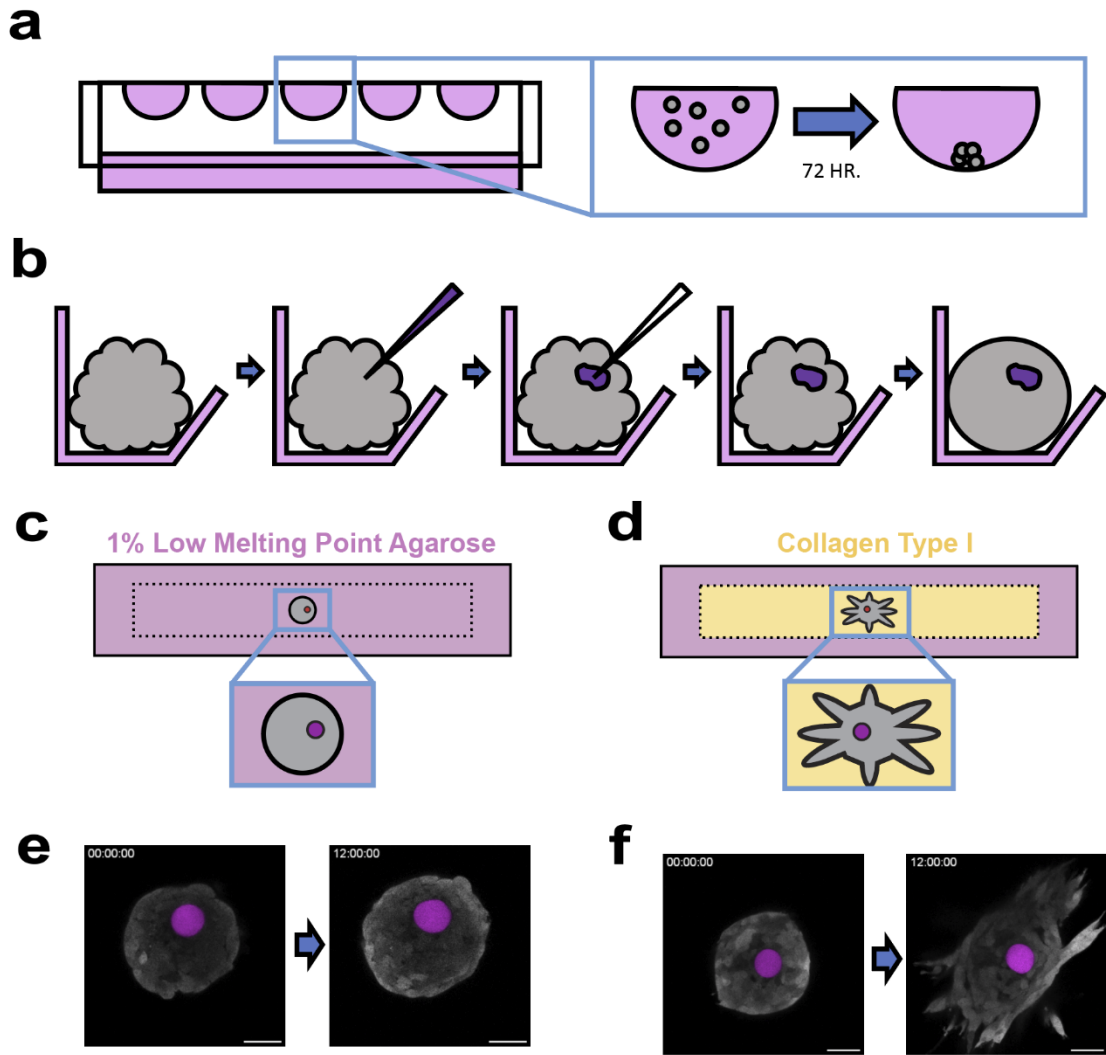


**Figure 1. Dual hydrogel cylindrical system to observe droplet-embedded spheroids.** **a**, Sketch depicting the hanging drop technique where several droplets containing a certain number of cells are placed on the lid of a petri dish and suspended over a reservoir of media. Left alone for 72 hours, the cells aggregate at the bottom of the droplet. **b**, Sketch depicting how oil is injected in the spheroid where the spheroid is in grey and the oil is in magenta. The spheroid is first placed in a well to make injection easier, the spheroid is then pierced without injecting the oil in, once the needle is ensured to be in the spheroid the oil is injected, the needle is pulled out and the spheroid is left to recover for a day. **c**, Sketch depicting the double hydrogel system in which the spheroid does not invade due to being encapsulated in agarose. **d**, Sketch depicting the double hydrogel system in which the spheroid does invade due to being encapsulated in collagen. **e**, Spheroid that was embedded in a system as shown in (c) at 0h and 12h. Scale bar, 50  $\mu\text{m}$ . **f**, Spheroid that was embedded in a system as shown in (d) at 0h and 12h. Scale bar, 50  $\mu\text{m}$ .

the chamber allows easy perfusion with fresh media (Methods). Spheroids embedded in agarose grew slightly in volume but were not able to invade their surroundings and remained largely spherical over the course of the experiment (Fig. 1c, e), as expected. In contrast, spheroids embedded in collagen I matrix readily invaded their surroundings (Fig. 1d, f). Just one hour after embedding the spheroid, small protrusions were already visible, indicating that the invasion process occurred very fast. After a few hours, cell streams (spheroid cellular protrusions) were observed extruding from the spheroid and bifurcating into multiple smaller streams. These results show that the dual hydrogel chamber enables the simultaneous 4D imaging of the invasion processes and the droplet force sensors.

In order to quantitatively characterize the invasion process, we developed a Python-based image analysis workflow for spheroid surface segmentation and protrusion tracking (Fig. 2a,b). Droplet-injected spheroids were imaged using confocal microscopy in 3D and time, and the surface of the spheroid was segmented at each timepoint (Methods). The 4D spheroid surface reconstruction allowed for a quantitative characterization of the invasion process. The tips of spheroid protrusions (invading cell streams) were first detected in the final image (latest timepoint) by analyzing high mean curvature regions on the spheroid surface and then tracked backwards in time (Fig. 2b), providing the trajectories and bifurcations (or branching points) of the cell streams during invasion (Fig. 2c,d). Using this analysis, it was possible to quantify the speed and spatial orientation of spheroid protrusions (Fig. 2e,f,g,h), the number and timing of bifurcations (Fig. 2i,j), their invasion distance and also the protrusion tip radius (Fig 2k,l). Moreover, by determining the spheroid's center of mass from the reconstructed surface it is possible to measure the principal direction of

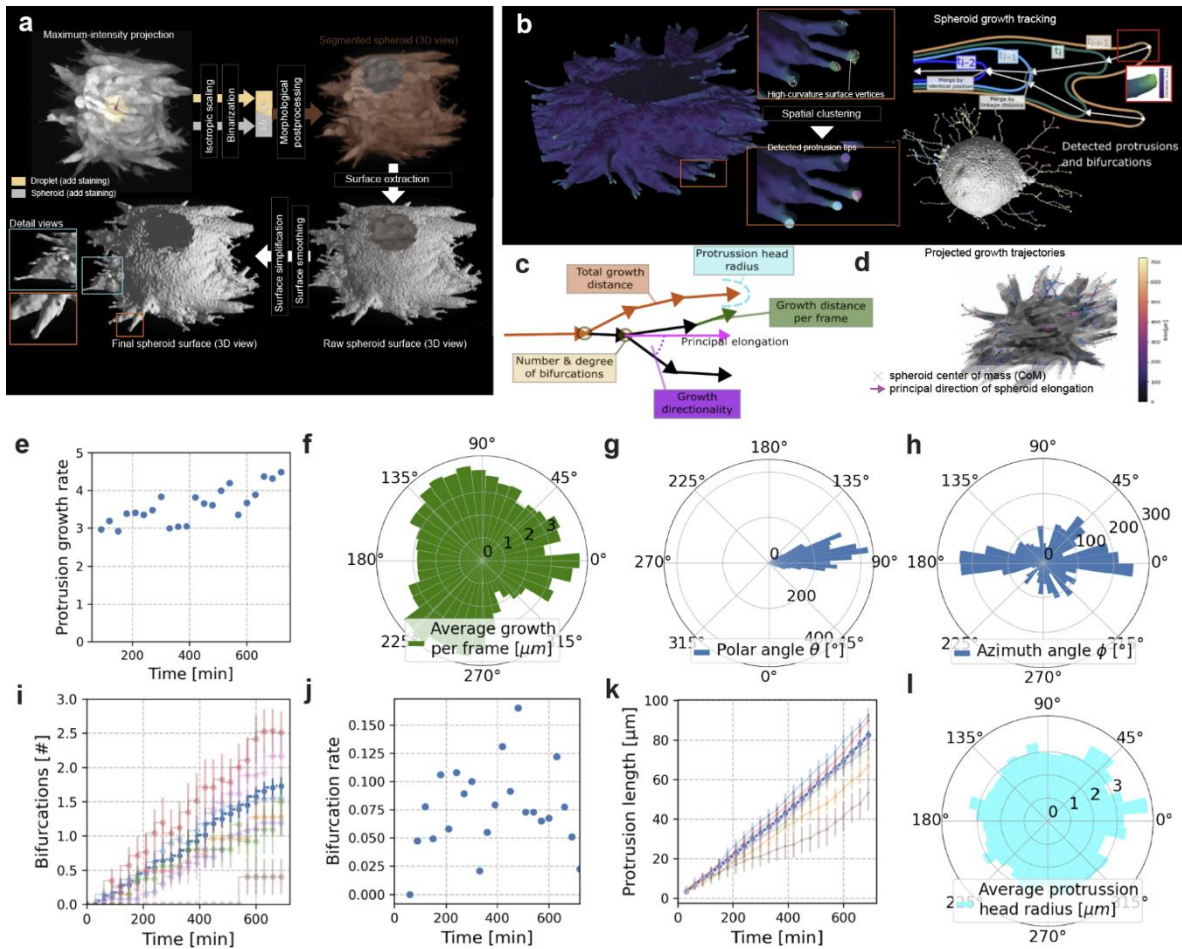


**Figure 2. Characterization of invading tumor spheroid.** **a**, Workflow for the reconstruction of the spheroid where 3D images are scaled and binarized, segmented, reconstructed, and then smoothed. **b**, Sketch depicting how invasive branches were traced back to their origin. **c**, Sketch demonstrating parameters that are measured from an individual invading spheroid. **d**, An overlay on a spheroid that demonstrates all the detected protrusions and bifurcations. **e**, Protrusion growth rate over time. **f**, Graph displaying the average growth rate of protrusions at different angles. **g**, Graph displaying the principal direction of invasion of collagen-embedded spheroids. **h**, Direction of protrusions and number of protrusions in that direction indicated by the length of the bar. **i**, Number of bifurcations over time. Dark blue line is the mean; all transparent colored lines are replicates. **j**, **k**, Average length of protrusion for an invading spheroid over time. Dark blue line is the mean; all transparent colored lines are replicates. **l**, Average protrusion head radius based on the direction of the protrusion.

invasion for each spheroid (Fig. 2g). Collectively, this dataset provides important information on the characteristics of the invasion process.

Our results show that protrusions elongate linearly with time, revealing an approximately constant protrusion speed (Fig. 2k). By measuring the preferred directions of invasion on a spherical coordinate system, we find that spheroid protrusions occur preferentially along the long axis of the cylindrical chamber, as revealed by the angular directions of the protrusions (Fig. 2g), indicating that cells avoid invasion along the paths closest to the surrounding agarose chamber. This may be caused by a mechanical anisotropy in the collagen network, as previously reported, or by cells perceiving other mechanical anisotropies [130]. Although it is reasonable to predict that the invading speed of each protrusion depends on their invasion direction, we found that protrusions in all directions grew at constant speed (Fig. 2f). Beyond the overall growth characteristics of invading tumor protrusions, each of the protrusions can split or bifurcate, thereby generating considerably more protrusions. The total number of bifurcations increases linearly over time as invasion proceeds, meaning that bifurcations appear at a constant rate (Fig. 2i,j). The size of the protrusion tips does not depend on the direction of invasion of the protrusions (Fig. 2l). Finally, protrusions with many bifurcations do not occur early-on in the invasion process, suggesting that protrusions need to reach a defined length before bifurcating (Fig. 2i).

### ***C. Endogenous mechanical stresses in non-invading and invading model tumors***

To monitor endogenous mechanical stresses inside tumor spheroids, we used oil microdroplets as stress sensors (Fig. 1c,d and Fig. 3a,b; Methods), as previously done in multiple living 3D tissues and 3D multicellular aggregates [123, 124, 125]. In order to quantify stresses with oil microdroplets, it is necessary to analyze the droplet deformations from 3D (or 4D) reconstructions of the droplet shape, which we obtained by 3D confocal

imaging of both non-invading and invading spheroids, as well as the droplets in them, for 12h (Fig. 3a,b). We used our previously developed STRESS software to reconstruct the surface of the droplets in 3D and time and quantify their surface geometry (Fig. 3c,d) [130]. Combined with measurements of the droplet's interfacial tension (Methods), the droplet surface geometry analysis provides quantitative measurements of the temporal evolution of the anisotropic stresses inside the spheroids and their temporal persistence.

The measured mechanical stress anisotropy inside the spheroids displayed marked differences in non-invading and invading spheroids (Fig. 3e). In agarose-embedded, non-invading tumor spheroids, the anisotropic stresses initially decreased until reaching a plateau and remained constant at approximately 700 Pa after that. In contrast, anisotropic stresses in collagen-embedded, invading tumor spheroids showed a sustained increase over time, from approximately 510 Pa to 810 Pa. While the magnitude of endogenous stresses showed clear differences in invading and non-invading tumor spheroids, the temporal persistence of stresses was very similar, as indicated by the temporal autocorrelation of the anisotropic stresses, which showed a fast initial decay (minutes) followed by a longer decay, indicating that a small component of the stresses persists over long timescales (several hours) in the tumors (Fig. 3f). Invading spheroids lose completely the stress memory in about 9 hours, but non-invading spheroids always show a small persistence (even at 12h), indicating that anisotropic stresses keep some mechanical memory of the initial stresses even after 12h. Beyond temporal persistence, spatial autocorrelation of the anisotropic stresses on the droplet surface shows periodic behavior over a length scale of approximately 5  $\mu\text{m}$ , a similar length scale as the cell size, suggesting that stresses at the cell scale may be dominant (Fig. 3g). The spatial correlation is lost over a length scale of approximately 15  $\mu\text{m}$ , meaning that

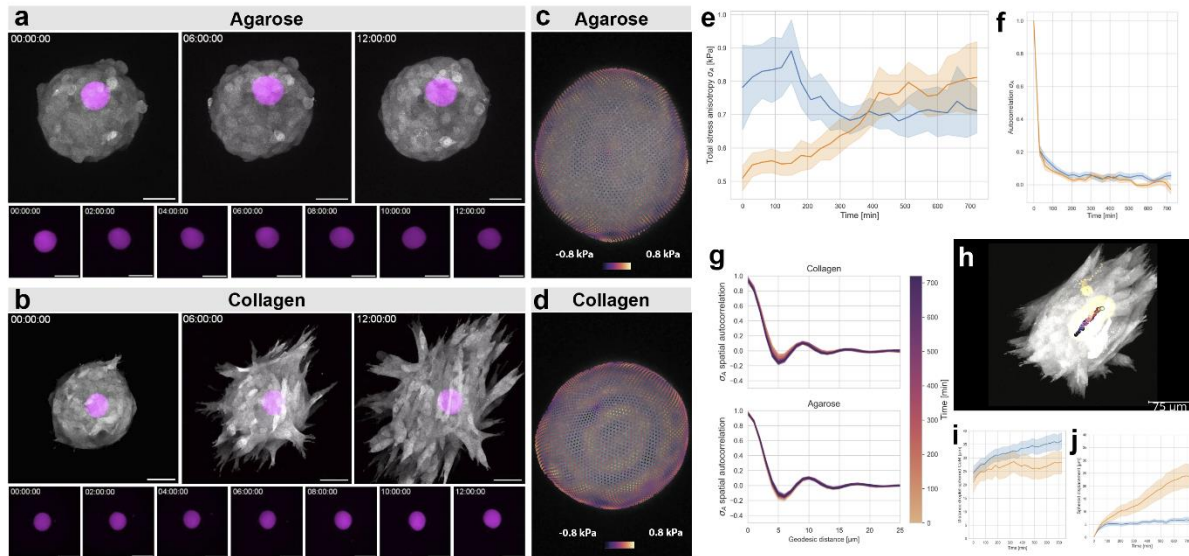


**Figure 3. Endogenous mechanical stresses inside non-invasive and invasive tumor spheroids.** **a**, Maximum intensity projection of spheroid with droplet injected embedded in 1% low melting point agarose at 0h, 6h, and 12h. Below is a maximum intensity projection of the droplet at 2h intervals. Scale bar, 50  $\mu\text{m}$ . **b**, Maximum projection of spheroid with droplet injected embedded in 2.7 mg/ml type I collagen at 0h, 6h, and 12h. Below is a maximum intensity projection of the droplet at 2h intervals. Scale bar, 50  $\mu\text{m}$ . **c**, Reconstruction of droplet embedded in a non-invasive tumor at 12h overlaid on original image. **d**, Reconstruction of droplet embedded in an invasive tumor at 12h overlaid on original image. **e**, Total stress anisotropy of droplets within non-invasive (blue,  $n = 10$ ) and invasive (orange,  $n = 7$ ) spheroids over 12h. **f**, Temporal autocorrelation of stresses in non-invasive (blue,  $n = 10$ ) and invasive (orange,  $n = 7$ ) spheroids over 12h. **g**, Spatial autocorrelation of stresses in non-invasive (agarose) and invasive (collagen) spheroids over 12h. **h**, Tracks showing how the center of the invasive spheroid and center of the droplet move throughout time. **i**, Distance between the center of mass of the droplet and spheroid in non-invasive (blue,  $n = 10$ ) and invasive (orange,  $n = 7$ ) spheroids over 12h. **j**, Displacement of non-invasive (blue,  $n = 10$ ) and invasive (orange,  $n = 7$ ) spheroids over 12h.

the dominant anisotropic stresses become uncorrelated in the tissue for distances larger than that. This indicates that the measured mechanical stresses become largely uncorrelated for distances of more than one cell size, a behavior that occurs in invasive and non-invasive tumors. Altogether, these results show that mechanical stress anisotropy increases substantially deep inside the tumor during tumor invasion, in contrast to non-invasive tumors, which show the opposite behavior.

Beyond mechanical stresses, the microdroplet can also be used as a passive tracer particle inside the tumor spheroid, which can provide information about the physical state of the tumor. We tracked both the center of mass of the droplet and the spheroid during invasion (Fig. 3h,i), as it is important to study the motion of the droplet relative to the spheroid. We found that in non-invading spheroids, both the droplet and the spheroid move less than the size of a single cell, approximately 10 microns, a result consistent with the tumor interior being solid-like. In contrast, the center of mass of invading tumors moves several cell sizes, approximately 30 microns, and so does the droplet too (Fig. 3i, j). The fact that the tissue moves by several cell sizes suggests a plastic, fluid-like flow inside the tumor during invasion, with the droplet being dragged by the flow, as the distance between the droplet and spheroid center of mass remains constant. These results suggest that the interior of non-invading and invading spheroids is in a different physical state, with the invasion process progressively fluidizing the tumor interior.

#### ***D. Supracellular stresses are low and constant in both invading and non-invading spheroids***

To understand whether the observed changes in mechanical stresses deep inside the tumor spheroids were due to supracellular stress propagation or changes of stresses at the cell scale, we decoupled these two contributions, as previously done using droplet stress sensors [131, 132]. The ellipsoidal deformation mode of the droplet provides information about the mechanical stress anisotropy at the length scale of the droplet, which ranges between 40 and 50  $\mu\text{m}$ , larger than the cell size (approximately 10  $\mu\text{m}$ ). This measurement averages out any spatial inhomogeneities in stresses below the size of the droplet, including

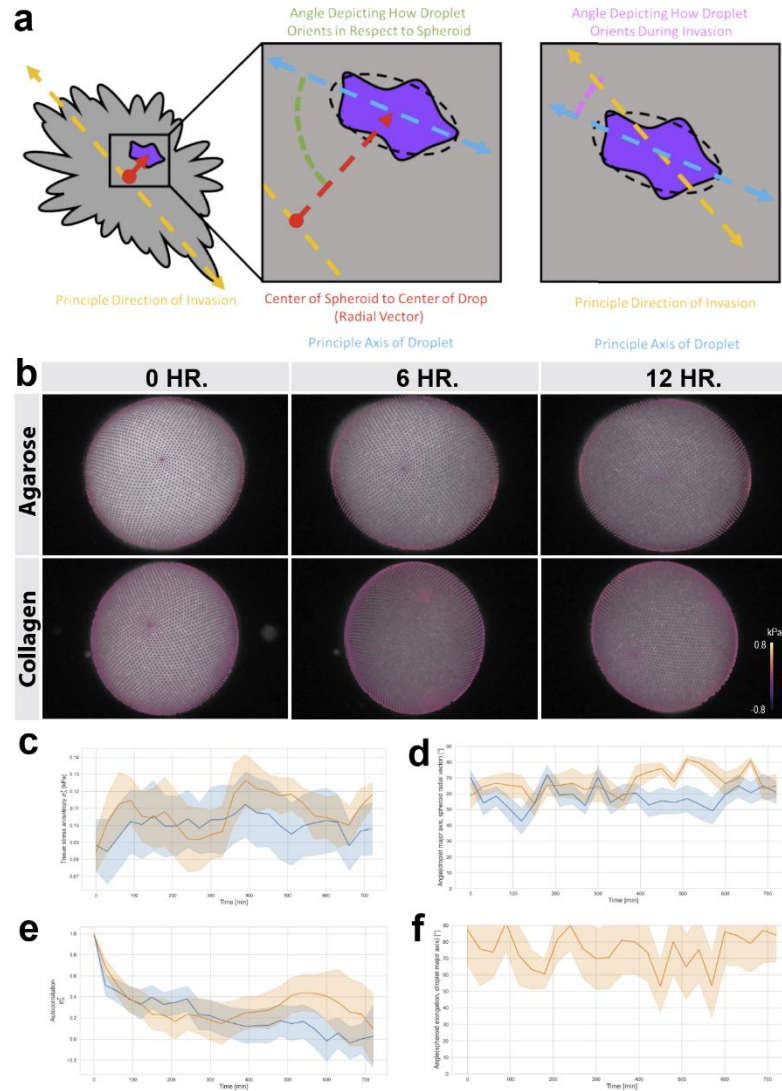


**Figure 4. Characteristics of mechanical stresses at the supracellular scale.** a, Sketch depicting the droplet and its ellipsoidal mode (black dashed line), the principal direction of invasion (yellow dashed line), the angle measured to depict the orientation of the droplet (green dashed line), and the angle measured to depict how the principal axis of the droplet orientation correlates with invasion (pink dashed line). b, Reconstruction of the supracellular mode of the droplet injected in invading (collagen) and non-invading (agarose) spheroids at 0h, 6h, and 12h. c, Supracellular-scale stress anisotropies of the droplet injected in the non-invading (blue,  $n = 10$ ) and invading (orange,  $n = 7$ ) spheroids over 12h. d, Radial projection of the droplet in the non-invading (blue,  $n = 10$ ) and invading (orange,  $n = 7$ ) spheroids over 12h. e, Temporal autocorrelation of supracellular-scale stresses in non-invading (blue,  $n = 10$ ) and invading (orange,  $n = 7$ ) spheroids over 12h. f, Angle between droplet principal axis and the principal direction of invasion in invading spheroids over 12h.

cell-sized variations in stress anisotropy, and provides instead a measure of the stresses at supracellular scales (Fig. 4a).

No differences between the measured values of supracellular stresses in non-invading and in invading tumor spheroids were found (Fig. 4b). In both conditions, supracellular stresses were low, ranging from 80 Pa to 120 Pa, and constant in time for the measurement period of 12h (Fig. 4c). Quantification of the angle between the long axis of droplet ellipsoidal deformation (principal axis with largest eigenvalue) and both the spheroid radial direction (from the spheroid center; spherical coordinates) and the global direction of tumor invasion shows that supracellular stresses are mostly perpendicular to the radial direction (Fig. 4a,d), as previously reported close to the spheroids surface, and do not orient along the global direction of tumor invasion (Fig. 4a,f) [127]. No differences were observed between non-invading and invading spheroids in the pattern of droplet orientation either (Fig. 4d), suggesting that supracellular stresses do not propagate from the surface to the tumor interior. Beyond magnitude and direction of supracellular stresses, we analyzed their persistence from their temporal autocorrelation. After an initial decay in the autocorrelation for about 2h, likely due to the settling of the spheroid after its initial embedding in the surrounding matrix, the temporal autocorrelation shows a very slow decay over the next 10h (Fig. 4e), indicating that supracellular stresses are very persistent and display memory of those low stresses over approximately 10h. Overall, these results show the existence of low, persistent stresses in tumor spheroids, with no observable differences between non-invading and invading tumor spheroids.

### *E. Cell-scale stresses are different in invading and non-invading tumors*

To obtain the endogenous mechanical stresses at the cell scale, we analyzed both the deviations of droplet deformations from the ellipsoidal deformation mode, as well as stress anisotropy at cellular scales (Fig. 5a,c). Stresses associated with deviations from the ellipsoidal mode were much larger than ellipsoidal stresses, dominating the total stresses reported above (Fig. 3e). Indeed, characterization of these stresses showed the same behavior as the total stresses reported above (Fig. 3e), including the differences in non-invading and invading tumor spheroids: in contrast to non-invading spheroids, for which stresses initially decrease and later remain constant, stresses associated to high order droplet deformation modes (deviation from ellipsoidal mode) increase over time for invading tumor spheroids (Fig. 5d). However, the temporal autocorrelation of these higher order stresses decays very fast, within less than 25 min, indicating that these stresses are very short lived (Fig. 5e). These results show that the measured total anisotropic stresses (Fig. 3e) includes two distinct contributions, one from low and persistent supracellular stresses and one from more rapidly changing and much larger higher order stresses. It is the higher order stresses, rather than supracellular stresses, that differ between non-invading and invading spheroids. Finally, since the spatial autocorrelation of higher order stresses also reveals spatial stresses inhomogeneities at the cellular scales (Fig. 5f), as the total stress anisotropy showed too (Fig. 3g), we analyzed the cell-scale stresses.

To understand if the differences in endogenous stresses between non-invading and invading tumors were occurring at the cell scale, we analyzed the differences in anisotropic stresses arising at cellular lengths scales on the droplet surface. To do so, we monitored the anisotropic stresses between adjacent maxima and minima in surface mean curvature (Fig.

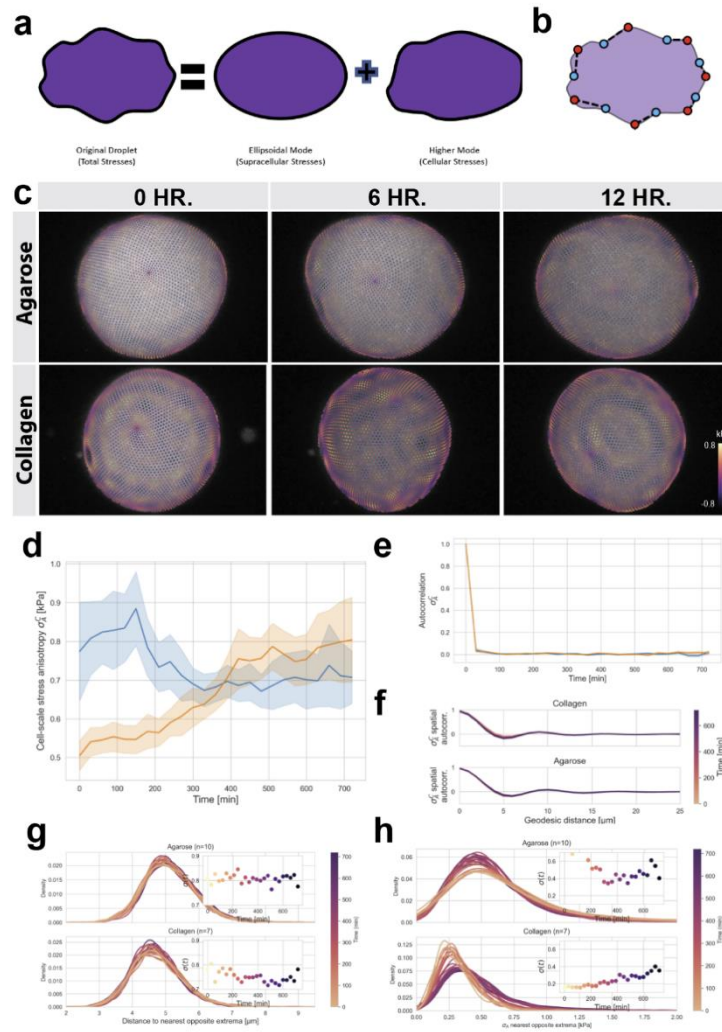


**Figure 5. Cellular stresses are different in invading and non-invading spheroids.** **a**, Sketch depicting how the reconstruction of the original droplet can be separated into different modes that can compose the original droplet. **b**, Simplified sketch demonstrating how the distance between hills-and-valleys is determined. Red dots as regions of high curvature and blue dots as regions of low curvature. Dashed lines between points are associated pairs of high and low regions. **c**, Reconstruction of the cellular mode of the droplet injected in invading (collagen) and non-invading (agarose) spheroids at 0h, 6h, and 12h. **d**, Cellular-scale stress anisotropies of the droplet injected in the non-invading (blue,  $n = 10$ ) and invading (orange,  $n = 7$ ) spheroids over 12h. **e**, Temporal autocorrelation of supracellular-scale stresses in non-invading (blue,  $n = 10$ ) and invading (orange,  $n = 7$ ) spheroids over 12h. **f**, Spatial autocorrelation of supracellular-scale stresses in non-invading (agarose) and invading (collagen) spheroids over 12h. **g**, Distance to the nearest opposite extrema in both non-invading (agarose) and invading (collagen) spheroids over 12h. Inset figure shows the standard deviation of the distributions over time. **h**, Distribution of stresses at each time point of non-invading (agarose) and invading (collagen) spheroids over 12 hours. Inset figure shows the standard deviation of the distributions over time.

5b). The geodesic distances between adjacent maxima and minima on the droplet surface are of approximately 5  $\mu\text{m}$  in non-invading and invading spheroids, respectively, as expected for inhomogeneities occurring at the cell scale (Fig. 5g). These results are in agreement with the spatial autocorrelation of the total stresses anisotropy, also showing a characteristic length scale of stress anisotropy at approximate 5  $\mu\text{m}$  (Fig. 3g). The distribution of endogenous cell-scale stresses displays opposing characteristics in invading and non-invading tumor spheroids (Fig. 5h). In non-invading, agarose-embedded tumors, average cell-scale stresses decay over time, and their variability, quantified by the standard deviation of their distribution, becomes considerably smaller over time, decreasing by about 2-fold. This indicates that cellular stresses in non-invading spheroids become more uniform and constant over time after approximately 3h in the agarose matrix. In contrast to non-invading spheroids, average cellular stresses in invading tumor spheroids increase over time and they become nearly 3-fold more variable. In addition, tracking the maximal cellular stresses by measuring the percentage of stresses over 1 kPa, we found that while the largest cellular stresses decrease over time in non-invading spheroids, they increase substantially in invading tumor spheroids. Altogether, these results show that the differences in endogenous mechanical stresses between non-invading and invading tumor spheroids originate at the cellular scale, with cellular stresses increasing both their magnitude and variability over time during tumor invasion.

### ***F. Discussion***

By directly measuring the endogenous mechanical stresses in the interior of non-invading and invading model tumors (4T1 murine breast cancer cell spheroids), as well as

quantifying the characteristics of the invasion process, we revealed that cellular stresses are different in invading tumors compared to their non-invading counterparts.

We found that total stresses increase in magnitude in invading spheroids compared to their non-invading counterpart and that this increase is due to the contributions from cell-scale forces. While other studies have measured the stresses inside spheroids that were encapsulated in a gel, they did not measure the stresses while the spheroid began to invade. In a study that was closely related although we were not using the same cancer cell type nor same microenvironment, what was observed was that over several days the total stresses did not change and averaged around 400 Pa (ranged from 200 Pa to 700 Pa) [126]. What is interesting about this is that both invading and non-invading spheroids revolve around this value, but their trends during this time period differ. Initially the non-invading spheroids start off at a higher stress value than the invading spheroids, but eventually plateau at around 700 Pa while the invading spheroids start at 500 Pa and increase to about 800 Pa. By decoupling the droplet to look at the contributions of cellular and supracellular forces, we found that supracellular stresses remained low while the contributions came from the cellular scale. This can potentially explain why the stresses in invading tumors increase as tumor undergoes massive phenotypic changes and the stresses increase initially when embedded as the cells continue to compact, but eventually plateau.

Additional to the increase in total stresses in invading spheroids, an increase in the variability of cell-scale stresses in invading spheroids was also observed. What we found was that in non-invading spheroids the variability of the stresses decreased through the course of the experiment and that invading spheroids had a narrow distribution of stresses that broadened as invasion continued. One could argue from these data that the spheroid is

in a more solid-like state when it is not invading and it starts to invade once the variability increases due to the fluidization of the tissue. It has been seen that variability in stresses is associated to tissue fluidization and that larger variability can more easily drive cellular rearrangements in otherwise solid-like tissues [131, 133].

From our data, it could be interpreted that the non-invading spheroids were in a solid-like state and that the invading spheroids were in a plastic-like state that was starting to fluidize as seen with its increase in variability of stresses. It is unlikely that the cause of this fluidization is related to the forces changing on the surface of the spheroid during invasion since the stresses are at the cell scale, but there could be other factors that warrant the cells in the immediate vicinity to apply stronger forces without moving the drop. One process that is upregulated during invasion and could explain this fluidization is the remodeling of the extracellular matrix. Remodeling of the extracellular matrix is due to the release of metalloproteases and it has been shown that enzymatic activity and expression increases with invasiveness [134]. It could be that the expression of metalloproteases that is occurring on the surface of the spheroid is also being propagated to the interior of the spheroid. The release of metalloproteases from surrounding cells next to the drop could lead to more cellular rearrangements and while this is occurring mostly at the surface the cells, it is slightly happening in the interior of the tumor allowing these variations in stresses to increase as invasion continues.

We additionally characterized the invasion process that was occurring in the spheroids. We found that the protrusions in our system grew linearly with time and at a constant speed. They were also oriented in a specific direction which could have arisen from the geometry of our dual hydrogel system. The protrusions always oriented in the long direction of the

cylindrical system and could be due to a mechanical feedback occurring during invasion. In other systems where spheroids are embedded in degradable extracellular matrix, the cells seem to invade radially [129]. The reason for this could be that there was little to no flow as the system was rigidifying as they are usually made in wells or petri dishes. It has been shown in previous research that by adding flow to collagen gels as they solidify, the collagen orientates in the direction of the flow causing spheroids to invade in specific directions [130]. In our system, since the spheroid was pulled into a capillary, it could be that the act of pulling the collagen into the tube reoriented the collagen fibers to induce this directional invasion.

It should be noted that in our system, we simplified our model so that we can lower the variables that could contribute to changes in mechanics. Spheroids have been shown to mimic the physiological properties of tumors, but they are vastly different. Real tumors contain a variety of cell types and the microenvironment contains more than one type of extracellular component. All these factors can influence how the tumor invades. Another aspect that is interesting to think about is why do these spheroids invade within hours versus in animals it can take months or years to invade. In our case, we stopped invasion by placing the spheroid in a matrix it cannot degrade, agarose. In animal systems, tumors have the ability to degrade and reorganize their surroundings, but they do not invade at the same rate. This study is aimed at furthering our knowledge of how stresses change during invasion, specifically of an *in vitro* tumor composed of one cell type in a specific microenvironment.

Overall, our results reveal the differences in endogenous mechanical stresses inside invading and non-invading tumors. Understanding these mechanical differences may help

the development of drugs targeting the molecular and cellular processes that control the observed mechanical changes during invasion.

### ***G. Methods***

#### **Cell culture and spheroid culture.**

Murine metastatic breast cancer cell line 4T1 was obtained from American Type Culture Collection. The cells were cultured under standard conditions (5% CO<sub>2</sub>, 37 C) in RPMI 1640 culture media (ThermoFisher, Cat #11875093) supplemented with 10% fetal bovine serum (Corning; Cat #35-011-CV) and 1% penicillin/streptomycin (VWR; Cat#16777-164). Cells were passaged every 2-3 days in a T-25 flask at a ratio of 1:10 using a 0.25% trypsin-EDTA solution (VWR; Cat #95053-260). The 4T1 cell line was additionally transfected with cytoplasmic GFP using a lentivirus [Essen Bioscience; Cat #4481] to allow for 3D reconstruction of the spheroid. A stable line was created by sorting using the Sony MA900 Fluorescence Cell Sorter and growing from a single cell. To make the spheroid, we utilized the hanging drop technique [135]. Petri dishes (FisherScientific; Cat #431761) with a height of 15 mm were used for this method. We placed 30 5  $\mu$ L droplets containing 100 cells on the inside of the lid. We then added 5 mL of media to the bottom portion of the dish to avoid evaporation of the droplets. We placed the lid back on the dish and placed it into the incubator for 3 days before harvesting them for experiments.

#### **Injection of oil into spheroids.**

Fresh injection pads were made using zebrafish microinjection molds (Adaptive Science Tools; Cat #PT-1) in sterile petri dishes before use. The media that was used for cell culture was also used to make the molds. About 5 mL of media was mixed with 2% agarose (Invitrogen; Cat # 16500100), heated, and poured into a petri dish. After it cooled, but not

solidified, the zebrafish microinjection mold was placed on top. Once solidified, the mold was removed and the pad was supplemented with media to cover the wells made. Spheroids were placed into individual wells using a pipette. The oil to be injected was Novec 7700 with 2% wt Krytox-PEG(600) (RAN Biotechnologies; Cat #008-FluoroSurfactant-1G) and 0.025mM FCy5 (a custom-made dye which was made as previously described) [136]. Needles were made from glass capillaries (World Precision Instrument; Cat # TW100F-4) pulled using the following parameters: Heat – 474; Pull – 200; Vel – 70; Delay – 40; Pressure – 200. Oil was backloaded into pulled needles using micropipette tips and mounted to an injection setup. We utilize a pico-liter injection station (Warner Instruments; Model PLI-100A Pico-Injector). Before injection, the tip was broken using tweezers and injection parameters were adjusted to allow the formation of a droplet of around 40-50  $\mu\text{m}$  in diameter. Once the spheroid was injected, it was left to culture for an additional day before embedding it in either 1% low melting point agarose (LMPA) or 2.7 mg/ml type 1 collagen. The collagen was made as in previous studies [137, 138].

### **Mounting of spheroids.**

Due to insertion of the oil droplet, the spheroid cannot be embed in as previous studies as the oil droplet causes the spheroid to sink before the substrate of choice solidifies. To this end, we developed a dual hydrogel system to overcome this issue. First, we prepared 1% LMPA and held it at 40°C until it was ready to be used; this will be used for the outer cylinder. Next, the inner cylinder solution is made (either 1% LMPA held at 40°C or 2.7 mg/ml type I collagen held on ice). Next, obtain 100  $\mu\text{L}$  of desired inner solution and insert an injected spheroid. The spheroid with the desired solution was pulled into a size 1 capillary (GmbH; Cat #701910) using its respective plunger. Using an upright microscope,

the sample can be rotated as the gel solidifies to ensure that it is in the middle of the capillary. Because of the small amount of reagent needed, the substrate will solidify within 5 minutes. To make the outer cylinder, place 100  $\mu$ L 1% LMPA on a sterile petri dish and extrude the encapsulated spheroid into the solution. Using a size 2 glass capillary (GmbH; Cat #701910) and its respective plunger, we pull the encapsulated spheroid along with the surrounding 1% LMPA and wait for the outer layer to solidify. Now that the spheroid is fully encapsulated, the dual hydrogel system can be placed on a 35mm glass bottom dish (MatTek; Cat #P35G-1.5-20-C) and filled it with media to perfuse the system. To ensure the sample did not move during imaging, a slice anchor (Warner Instruments; Cat #64-0266) was placed on top of the system.

#### **Imaging of tumor spheroids.**

Spheroids were imaged one hour after insertion in the dual hydrogel system. A laser scanning confocal microscope (LSM 710 Zeiss Inc.) equipped with a 25x water immersion lens (Zeiss; LD LCI Plan-Apochromat 25x/0.8 Imm Corr DIC M27) was used to obtain images of the spheroid and their embedded droplet. The incubation chamber on the confocal microscope maintained the temperature at 37°C and 5% CO<sub>2</sub> during the course of the experiment. 3D imaging was acquired at 30-minute intervals for a total period of 12h at full confocality (1AU; 1.2  $\mu$ m z-steps) to capture the droplet and spheroid for both the invading and non-invading cases.

#### **Segmentation of the spheroid surface and tracking of invading protrusions.**

As a first step, the image data which consists of two-color channels (fluorescently labelled droplet and spheroid), were first rescaled to isotropic voxel sizes. The rescaled spheroid and droplet image data were then processed with a median smoothing and

binarized with the mean- and Otsu-threshold methods, respectively [139]. The resulting label images were merged with a binary or operation. Morphological post-processing (i.e., binary closing and removal of small objects) was applied to obtain a single, labelled object for each timepoint. The marching cubes algorithm was then applied to obtain a surface representation of the spheroid in every timepoint. Lastly, the generated surface mesh was smoothed with a smoothing filter and a decimation method in order to create a manageable number of vertices. We used the clesperanto, scikit-image and vedo Python libraries for the described workflow steps [140, 141, 142].

For this, we measured the approximate local curvature on the spheroid's surface by fitting a sphere to all neighboring vertices of a given surface within a defined radius. The local curvature can then be estimated as the squared inverse of the determined radius. A manually chosen threshold then allows to identify a selection of points that are located on and around the protrusion heads. We aggregated these groups points into single points for each protrusion head by means of the DBSCAN clustering algorithm as implemented in the Python library scikit-learn based on the delineated point's coordinates [143]. The inverse growth trajectories could then be established by determining each protrusion head's respective closest point in the surface mesh in the previous timestep (Fig. 2b). We then aggregate the determined points into a graph network structure with the networkx Python package, which allows us to derive quantitative characteristics regarding branching behavior with respect to time [144]. Fig. 2c and 2d show an overview of the derived quantities and an example of aggregated growth trajectories overlaid with a maximum-z projection of the spheroid's final observed timeframe, respectively.

### **Quantification of mechanical stresses using oil microdroplets.**

Stresses were quantified from deformations of the oil droplets inserted into the spheroids. To obtain the deformations, the droplets were imaged in 3D using confocal microscopy and reconstructed using the previously developed STRESS software [132]. The interfacial tension of the droplet in cell culture media was measured using a pendant drop tensiometer (Biolin Scientific; Attension), as previously described [125]. The interfacial tension value we obtained for the oil droplets in agarose-embedded spheroids was  $5.35 \pm 0.35$  mN/m and for oil droplets in collagen-embedded spheroids was  $5.06 \pm 0.16$  mN/m. With the interfacial tension and voxel size of the images known, the software can be utilized to measure the stresses of droplets at each time point. Using spherical harmonics, the droplet can further be analyzed by separating the ellipsoid mode to look at supracellular stresses and the deviations from this mode to look at cellular scale stresses.

## IV. Conclusion

In this thesis, two different approaches were used to further our understanding of mechanics during two different biological processes: (1) mating projection growth; and (2) invasion (the initial stage of metastatic growth). While we have gained a better understanding of these two processes, there are still many questions left unanswered.

### *Unicellular System: Mating Projection Growth in S. cerevisiae*

In order to investigate the theoretical model made in Chapter 2, we deleted several components of the CWI pathway to test specific predictions about tip stability and shape, but this model did not provide any information about positional information of molecular machinery, specifically the machinery required for the event right before tip morphogenesis, polarization. As a potential future direction, we were interested in decoupling tip growth from polarization. Cell polarity is crucial for a variety of cellular processes in eukaryotes. In *S. cerevisiae*, it is required not only for proper budding, but also mating projection growth. Two major components required to coordinate these changes are Rho1 and Cdc42. Each of these components controls a variety of downstream processes, but they both converge onto Bni1, a formin shown to regulate the actin cytoskeleton. As the CWI pathway is responsible for sensing the mechanical changes in the wall, our hypothesis is that Cdc42 is primarily responsible for the polarization aspect of tip growth. It is known that Cdc42 and Rho1 have overlapping binding sites with Bni1. In order to investigate this further, we would like to cause specific point mutations to disrupt the binding interaction between Rho1-Bni1, the interaction that is coupled to interpreting the mechanical state of the cell wall. The purpose of this study would be to investigate how mechanical feedback impinges on cell polarization and to further our understanding of polarization during mating projection growth.

*Multicellular System: Initial Stages of Metastatic Growth in 4T1 Spheroids*

When we originally set forth to doing the work in Chapter 3, we were aiming to fill a gap in our understanding of how mechanical stresses in tumors change as they begin to invade. Previous work had already investigated how much force is being applied to the environment by the use of spheroids and also how much force individual cancer cells can apply by using cells of varying malignancy, but none have quantified how the forces change in an invading tumor. To address this, we utilized fluorescent bioinert microdroplets and injected them into spheroids. By placing the spheroids into collagen type I matrices, we were able to induce invasion and observe how the forces change during the process. Upon measurement, we saw that the forces on the droplet increased over the span of the invasion while the forces of the droplet stayed constant in the non-invading case. This was an interesting result as it demonstrates how the forces within the tumor can potentially correlate with the stresses being applied on its surrounding.

While we found that the forces on the droplet were increasing as invasion was happening, the mechanism remains unknown. As potential future directions, we were interested in understanding why the droplets would experience differences in stresses whether it was invading or not. One method to assess why the stresses would differ in the invading case versus the non-invading case is by looking at the nuclear movement of the cells during both cases. Our idea is to understand if the environment directly around the droplet is changing, we have a hypothesis that the cells are not moving or migrating in the non-invading case as much as the cells of the invading case during the span of the experiment. If the cells are not moving, then the force would stay constant and would explain why the droplet does not read any changes. From our observations, it was also noted

that the droplet stayed in the same relative area regardless if the spheroid was invading or not, the differences in stresses could be from the movement of the surrounding cells, but its locked location could be from being encapsulated extracellular matrix. While interesting to also investigate and more difficult experimentally, it would be novel to see how the stresses in the spheroid correlate with the stresses being applied to the surrounding. For now, doing these types of experiments would elaborate on our result.

Understanding how mechanics change as growth occurs in different biological settings requires an immense collaboration of disciplines and techniques. Our studies demonstrate that whether we are looking at individual cells or a multitude of cells, there is always more we can understand. The conclusions of the processes we studied in these cases go to show that the mechanics of a system are never as they seem and can bring about new concepts we did even know existed.

## References

1. D.W.T Thompson. *On Growth and Form*. Cambridge University Press, 1917.
2. E.B. Wilson. *The Cell in Development and Heredity*. Macmillan, New York, ed. 3, 1925.
3. A.M. Turing. The chemical basis of morphogenesis. *Phil. Trans. R. Soc. Lond. B.* 237:37–72, 1952.
4. H. De Belly, E.K. Paluch, K.J. Chalut. Interplay between mechanics and signalling in regulating cell fate. *Nat. Rev. Mol. Cell Bio.* 23: 465-80, 2022.
5. I. Dasgupta, D. McCollum. Control of cellular responses to mechanical cues through YAP/TAZ regulation. *JBC Reviews* 294(46): P17693-17706, 2019.
6. A.A. Anlaş, C.M. Nelson. Tissue mechanics regulates form, function, and dysfunction. *Curr. Opin. Cell Bio.* 54: 98-105, 2018.
7. E. Trubuil, A. D'Angelo, J. Solon. Tissue mechanics in morphogenesis: active control of tissue material properties to shape living organisms. *Cell & Development* 168: 203777, 2021.
8. G. Battilana, F. Zanconato, S. Piccolo. Mechanisms of YAP/TAZ transcriptional control. *Cell Stress* 5(11): 167-172, 2021.
9. J.Z. Kechagia, J. Ivaska, P. Roca-Cusachs. Integrins as biomechanical sensors of the microenvironment. *Nat. Rev. Mol. Cell Bio.* 20: 257-473, 2019.
10. O. Campàs. A toolbox to explore the mechanics of living embryonic tissues. *Sem. In Cell & Dev. Bio.* 55: 119-130, 2016.
11. W.J. Polacheck, C.S. Chen. Measuring cell-generated forces: a guide to the available tools. *Nat Methods* 13(5): 415-423, 2016.
12. P. Egan, R. Sinko, P.R. LeDuc, S. Keten. The role of mechanics in biological and bio-inspired system. *Nat. Comm.* 6: 7418, 2015.
13. E. Farge. Mechanical induction of Twist in the *Drosophila* foregut/stomodaeal primordium. *Current Bio* 13(16): 1365-1377, 2003.
14. E.K. Paluch, C.M. Nelson, N. Biais, B. Fabry, J. Moeller, B.L. Pruitt, C. Wollnik, G. Kudryasheva, F. Rehfeldt, W. Federle. Mechanotransduction: use the force(s). *BMC Biol* 13: 47, 2015.
15. V.M. Weaver. Cell and tissue mechanics: the new cell biology frontier. *Mol Biol Cell* 28(14): 1815-18, 2017.
16. G. Salbreux, G. Charras, E. Paluch. Actin cortex mechanics and cellular morphogenesis. *Trends Cell Biol* 22(10): 536-45, 2012.

17. F.M. Harold. To shape a cell: an inquiry into the causes of morphogenesis of microorganisms. *Microbiol Rev* 54(4): 381-431, 1990.
18. H-O Park, & E. Bi. Central role of small GTPases in the development of cell polarity in yeast and beyond. *Microbiol Mol Biol Rev* 71(1): 48-96, 2007.
19. D. Pruyne, A. Bretscher. Polarization of cell growth in yeast I. Establishment and maintenance of polarity states. *J Cell Sci* 113(Pt 3): 365-375, 2000.
20. M. Evangelista, K. Blundell, M.S. Longtine, C.J. Chow, N. Adames, J.R. Pringle, M. Peter, C. Boone. Bni1p, a yeast formin linking Cdc42p and the actin cytoskeleton during polarized morphogenesis. *Science* 276(5309): 118-122, 1997.
21. D.J. Adams. Fungal cell wall chitinases and glucanases. *Microbiology* 150(Pt 7): 2029-35, 2004.
22. O. Campàs, L. Mahadevan. Shape and dynamics of tip-growing cells. *Curr Biol* 19(24): 2102-2107, 2009.
23. G. Bell, A.O. Mooers. Size and complexity among multicellular organisms. *Bio. Jour. Of the Lin. Soc.* 60(3): 345-363, 1997.
24. L.A. Torre, F. Bray, R.L. Siegel, J. Ferlay, J. Lortet-Tieulent, A. Jemal. Global cancer statistics. *CA Cancer J Clin* 65(2): 87-108, 2015.
25. E.Y.H.P. Lee, W.J. Muller. Oncogenes and tumor suppressor genes. *Cold Spring Harb Perspect Biol.* 2(10): a003236, 2010.
26. C. Kandoth, M.D. McLellan, F. Vandin, K. Ye, B. Niu, C. Lu, M. Xie, Q. Zhang, J.F. McMichael, M.A. Wyczalkowski, M.D.M. Leiserson, C.A. Miller, J.S. Welch, M.J. Walter, M.C. Wendl, T.J. Ley, R.K. Wilson, B.J. Raphael, L. Ding. Mutational landscape and significance across 12 major cancer types. *Nature* 502: 333-339, 2013.
27. R.C. Lilenbaum, M.R. Green. Novel chemotherapeutic agents in the treatment of non-small-cell lung cancer. *J Clin Oncol.* 11(7):1391-402, 1993.
28. Y. Oku, N. Nishiya, T. Shito, R. Yamamoto, Y. Yamamoto, C. Oyama, Y. Uehara. Small molecules inhibiting the nuclear localization of YAP/TAZ for chemotherapeutics and chemosensitizers against breast cancers. *FEBS Open Bio* 5: 542-549, 2015.
29. H. Dillekås, M.S. Rogers, O. Straume. Are 90% of deaths from cancer caused by metastases? *Cancer Med.* 8(12): 5574-5576, 2019.
30. C.L. Chaffer, R.A. Weinberg. A perspective on cancer cell metastasis. *Science* 331(6024): 1559-1564, 2011.
31. D. Hanahan, R.A. Weinberg. Hallmarks of cancer: the next generation. *Cell* 144(5): 646-674, 2011.

32. J. Chang, O. Chaudhuri. Beyond proteases: basement membrane mechanics and cancer invasion. *J. Cell Bio.* 218(8): 2456-2469, 2019.
33. J. Fares, M.Y. Fares, H.H. Khachfe, H.A. Salhab, Y. Fares. Molecular principles of metastasis: a hallmark of cancer revisited. *Sig Transduct Target Ther* 5(28), 2020.
34. R. Naomi, P.M. Ridzuan, H. Bahari. Current insights into collagen type I. *Polymers (Basel)* 13(16): 2642, 2021.
35. E.A. Aisenbrey, W.L. Murphy. Synthetic alternatives to Matrigel. *Nat Rev Mater.* 5(7): 539-551, 2020.
36. P. Roca-Cusachs, V. Conte, X. Trepap. Quantifying forces in cell biology. *Nature Cell Biology* 19: 742-751, 2017.
37. O. Campàs. A toolbox to explore the mechanics of living embryonic tissues. *Semin Cell Dev Biol* 55: 119-130, 2016.
38. E. Mohagheghian, J. Luo, J. Chen, G. Chaudhary, J. Chen, J. Sun, R.H. Ewoldt, N. Wang. Quantifying compressive forces between living cell layers and within tissues using elastic round microgels. *Nature Communication* 9: 1878, 2018.
39. F. Serwane, A. Mongera, P. Rowghanian, D.A. Kealhofer, A.A. Lucio, Z.M. Hockenbery, O. Campàs. *In vivo* quantification of spatially varying mechanical properties in developing tissues. *Nat Methods* 14(2): 181-186, 2017.
40. A.A. Lucio, A. Mongera, E. Shelton, R. Chen, A. Doyle, O. Campàs. Spatiotemporal variation of endogenous cell-generated stresses within 3D multicellular spheroids. *Scientific Reports* 7: 12022, 2017.
41. A. Engler, P. Humbert, B. Wehrle-Haller, V. Weaver. Multiscale modeling of form and function. *Science* 324(5924): 208–212, 2009
42. K. Young. The selective value of bacterial shape. *Microbiology and molecular biology reviews: MMBR* 70(3): 660–703, 2006.
43. W. Nelson. Adaptation of core mechanisms to generate cell polarity. *Nature* 422(6933): 766–774, 2003.
44. E. Cabib, J. Arroyo. How carbohydrates sculpt cells: chemical control of morphogenesis in the yeast cell wall. *Nature Reviews Microbiology* 11(9):648–655, 2013.
45. A. Geitmann, J. Ortega. Mechanics and modeling of plant cell growth. *Trends in Plant Science* 14(9):467–478, 2009.
46. F. Harold. Force and compliance: rethinking morphogenesis in walled cells. *Fungal Genetics and Biology: FG & B* 37(3):271–282, 2002.

47. S.P. Banavar, C. Gomez, M. Trogdon, L.R. Petzold, T-M Yi, O. Campàs. Mechanical feedback coordinates cell wall expansion and assembly in yeast mating morphogenesis. *PLoS Comput Biol* e1005940-19, 2018.
48. F. Harold. Molecules into cells: specifying spatial architecture. *Microbiology and Molecular Biology Reviews: MMBR* 69(4): 544–564, 2005
49. J. Kroeger, A. Geitmann. The pollen tube paradigm revisited. *Current Opinion in Plant Biology* 15(6): 618–624, 2012
50. R. Lew. How does a hypha grow? The biophysics of pressurized growth in fungi. *Nature Publishing Group* 9(7): 509–518, 2011.
51. R. Bernal, E. Rojas, J. Dumais. The mechanics of tip growth morphogenesis: what we have learned from rubber balloons. *JOMMS* 2(6): 1157–1168, 2007.
52. B. Goodwin, L. Trainor. Tip and Whorl Morphogenesis in *Acetabularia* by Calcium-Regulated Strain Fields. *Journal of Theoretical Biology* 117: 79–106, 1985.
53. S. Bartnicki-Garcia, F. Hergert, G. Gierz. Computer simulation of fungal morphogenesis and the mathematical basis for hyphal (tip) growth. *Protoplasma* 153, 1989.
54. S. Tindemans, N. Kern, B. Mulder. The diffusive vesicle supply center model for tip growth in fungal hyphae. *Journal of Theoretical Biology* 238(4): 937–948, 2006.
55. A. Goriely, M. Tabor. Self-Similar Tip Growth in Filamentary Organisms. *Phys Rev Lett* 90(10): 108101–4, 2003.
56. J. Lockhart. An Analysis of Irreversible Plant Cell Elongation. *Journal of Theoretical Biology* 8: 264–275, 1965.
57. B. Goldenbogen, W. Giese, M. Hemmen, J. Uhlendorf, A. Herrmann, E. Klipp. Dynamics of cell wall elasticity pattern shapes the cell during yeast mating morphogenesis. *Open Biology*. 6(9): 160136–14, 2006.
58. J. Abenza, E. Couturier, J. Dodgson, J. Dickmann, A. Chessel, J. Dumais, R.E.C. Salas. Wall mechanics and exocytosis define the shape of growth domains in fission yeast. *Nature Communications* 6: 1–13, 2015.
59. T. Drake, D. Vavylonis. Model of Fission Yeast Cell Shape Driven by Membrane-Bound Growth Factors and the Cytoskeleton. *PLoS Computational Biology* 9(10): e1003287, 2013.
60. O. Campàs, L. Mahadevan. Shape and Dynamics of Tip-Growing Cells. *Current Biology* 19(24): 2102–2107, 2009.

61. L. Merlini. Mate and fuse: how yeast cells do it. *Open Biology* 3(3):130008–130008, 2013.
62. E. Bi, H. Park. Cell Polarization and Cytokinesis in Budding Yeast. *Genetics* 191(2): 347–387, 2012.
63. D. Pruyne, A. Bretscher. Polarization of cell growth in yeast: I. Establishment and maintenance of polarity states. *J Cell Sci* 113: 365–375, 2000.
64. M. Evangelista, K. Blundell, M.S. Longtine, C. Chow, N. Adames, J.R. Pringle, M. Peter, C. Boone. Bni1p, a yeast formin linking Cdc42p and the actin cytoskeleton during polarized morphogenesis. *Science* 276(5309): 118–122, 1997.
65. M. Snyder. The Spa2 Protein of Yeast Localizes to Sites of Cell-Growth. *The Journal of Cell Biology* 108(4): 1419–1429, 1989.
66. S. Bidlingmaier, M. Snyder. Regulation of polarized growth initiation and termination cycles by the polarisome and Cdc42 regulators. *The Journal of Cell Biology* 164(2): 207–218, 2004.
67. D. TerBush, T. Maurice, D. Roth, P. Novick. The Exocyst is A Multiprotein Complex Required For Exocytosis In *Saccharomyces Cerevisiae*. *Embo Journal* 15(23): 64883–66494, 1996
68. D.E. Levin. Cell wall integrity signaling in *Saccharomyces cerevisiae*. *Microbiology and Molecular Biology Reviews* 69(2): 262–291, 2005.
69. R. Rodicio, J. Heinisch. Together we are strong—cell wall integrity sensors in yeasts. *Yeast* 27(8): 531–540, 2010.
70. D. Levin. Regulation of Cell Wall Biogenesis in *Saccharomyces cerevisiae*: The Cell Wall Integrity Signaling Pathway. *Genetics* 189(4): 1145–1175, 2011.
71. C. Kock, Y.F. Dufrière, J.J. Heinisch. Up against the Wall: Is Yeast Cell Wall Integrity Ensured by Mechanosensing in Plasma Membrane Microdomains? *Appl Environ Microbiol* 81(3):806–811, 2015.
72. J. Verna, A. Lodder, K. Lee, A. Vagts, R. Ballester. A family of genes required for maintenance of cell wall integrity and for the stress response in *Saccharomyces cerevisiae*. *Proceedings of the National Academy of Sciences* 94(25): 13804–13809, 1997.
73. B.D. Manning, R. Padmanabha, M. Snyder. The Rho-GEF Rom2p Localizes to Sites of Polarized Cell Growth and Participates in Cytoskeletal Functions in *Saccharomyces cerevisiae*. *Molecular Biology of the Cell* 8(10): 1829–1844, 1997.
74. B. Philip, D. Levin. Wsc1 and Mid2 Are Cell Surface Sensors for Cell Wall Integrity Signaling That Act through Rom2, a Guanine Nucleotide Exchange Factor for Rho1. *Mol Cell Biol* 21(1): 271–280, 2001.

75. P. Perez, S.A. Rincón. Rho GTPases: regulation of cell polarity and growth in yeasts. *Biochem J* 426(3): 243–253, 2010.
76. V. Dupres, D. Alsteens, S. Wilk, B. Hansen, J. Heinisch, Y. Dufrêne. The yeast Wsc1 cell surface sensor behaves like a nanospring *in vivo*. *Nat Chem Biol* 5(11): 857–862, 2009.
77. A. Straede, J. Heinisch. Functional analyses of the extra- and intracellular domains of the yeast cell wall integrity sensors Mid2 and Wsc1. *FEBS Letters* 581(23): 4495–4500, 2007.
78. F. Hutzler, R. Gerstl, M. Lommel, S. Strahl. Protein N-glycosylation determines functionality of the *Saccharomyces cerevisiae* cell wall integrity sensor Mid2p. *Mol Microbiol* 68(6): 1438–1449, 2008.
79. T. Ono, T. Suzuki, Y. Anraku, H. Iida. The MID2 gene encodes a putative integral membrane protein with a Ca<sup>2+</sup>-binding domain and shows mating pheromone-stimulated expression in *Saccharomyces cerevisiae*. *Gene* 151: 203–208, 1994.
80. T. Ketela, R. Green, H. Bussey. *Saccharomyces cerevisiae* Mid2p Is a Potential Cell Wall Stress Sensor and Upstream Activator of the PKC1-MPK1 Cell Integrity Pathway. *Journal of Bacteriology* 181(11): 3330–3340, 1999.
81. M. Rajavel, B. Philip, B. Buehrer, B. Errede, D. Levin. Mid2 Is a Putative Sensor for Cell Integrity Signaling in *Saccharomyces cerevisiae*. *Mol Cell Biol* 19(6): 3969–3976, 1999.
82. B. Chapa-y Lazo, E. Allwood, I. Smaczynska-de Rooij, M. Snape, K. Ayscough. Yeast Endocytic Adaptor AP-2 Binds the Stress Sensor Mid2 and Functions in Polarized Cell Responses. *Traffic* 15(5): 546–557, 2014.
83. C. Guthrie, G. Fink. Guide to yeast genetics and molecular biology. *Methods in Enzymology* 194: 1–863, 1991.
84. U. Gueldener, J. Heinisch, G.J. Koehler, D. Voss, J.H. Hegemann. A second set of loxP marker cassettes for Cre-mediated multiple gene knockouts in budding yeast. *Nucleic Acids Res.* 30: e23, 2003.
85. F. Klis, C. de Koster, D. Brul. Cell Wall-Related Bionumbers and Bioestimates of *Saccharomyces cerevisiae* and *Candida albicans*. *Eukaryotic Cell* 13(1): 2–9, 2014.
86. C. Chou, T. Moore, S. Chang, Q. Nie, T. Yi. Signaling regulated endocytosis and exocytosis lead to mating pheromone concentration dependent morphologies in yeast. *FEBS Letters* 586(23): 4208–4214, 2012.
87. B. Van De Fliert, P. Howell, J. Ockenden. Pressure-driven flow of a thin viscous sheet. *J Fluid Mech* 292: 359–376, 1995.

88. M. Bosch, P.K. Hepler. Pectin methylesterases and pectin dynamics in pollen tubes. *The Plant Cell* 17(12): 3219–3226, 2005.
89. P. Fayant, O. Girlanda, Y. Chebli, C.E. Aubin, I. Villemure, A. Geitmann. Finite Element Model of Polar Growth in Pollen Tubes. *Plant Cell* 22(8): 2579–2593, 2010.
90. D.J. Adams. Fungal cell wall chitinases and glucanases. *Microbiology* 150(7): 2029–2035, 2004.
91. C. Douglas, F. Foor, J. Marrinan, N. Morin, J. Nielsen, A. Dahl, P. Mazur, W. Baginsky, W. Li, M. el-Sherbeini. The *Saccharomyces Cerevisiae* Fks1 (Etg1) Gene Encodes an Integral Membrane-Protein Which Is a Subunit of 1,3-Beta-D-Glucan Synthase. *Proceedings of the National Academy of Sciences* 91(26): 12907–12911, 1994.
92. T. Utsugi, M. Minemura, A. Hirata, M. Abe, D. Watanabe, Y. Ohya. Movement of yeast 1,3-beta-glucan synthase is essential for uniform cell wall synthesis. *Genes to Cells*. 7(1): 1–9, 2002.
93. P. Delley, M. Hall. Cell Wall Stress Depolarizes Cell Growth Via Hyperactivation of RHO1. *The Journal of Cell Biology* 147(1): 163–174, 1999.
94. Abe M, H. Qadota, A. Hirata, Y. Ohya. Lack of GTP-bound Rho1p in secretory vesicles of *Saccharomyces cerevisiae*. *The Journal of Cell Biology* 162(1): 85–97, 2003.
95. M. Jose, S. Tollis, D. Nair, J. Sibarita, D. McCusker. Robust polarity establishment occurs via an endocytosis-based cortical corralling mechanism. *The Journal of Cell Biology* 200(4): 407–418, 2013.
96. J. Valdez-Taubas, H. Pelham. Slow Diffusion of Proteins in the Yeast Plasma Membrane Allows Polarity to Be Maintained by Endocytic Cycling. *Current Biology* 13(18): 1636–1640, 2003.
97. L. Huberman, A. Murray. A Model for Cell Wall Dissolution in Mating Yeast Cells: Polarized Secretion and Restricted Diffusion of Cell Wall Remodeling Enzymes Induces Local Dissolution. *PLoS ONE* 9(10), 2014.
98. L. Carrillo, B. Cucu, V. Bandmann, U. Homann, B. Hertel, S. Hillmer, G. Thiel, A. Bertl. High-Resolution Membrane Capacitance Measurements for Studying Endocytosis and Exocytosis in Yeast. *Traffic* 16(7): 760–772, 2015.
99. F. Finger, T. Hughes, P. Novick. Sec3p Is a Spatial Landmark for Polarized Secretion in Budding Yeast. *Cell* 92(4): 559–571, 1998.
100. R. Teparić, V. Mrša. Proteins involved in building, maintaining and remodeling of yeast cell walls. *Current Genetics* 59(4): 171–185, 2013.

101. N. Röckel, S. Wolf, B. Kost, T. Rausch, S. Greiner. Elaborate spatial patterning of cell-wall PME and PMEI at the pollen tube tip involves PMEI endocytosis, and reflects the distribution of esterified and de-esterified pectins. *Plant J* 53(1): 133–143, 2008.
102. K. Huang, R. Mukhopadhyay, B. Wen, Z. Gitai, N. Wingreen. Cell shape and cell-wall organization in Gram-negative bacteria. *Proceedings of the National Academy of Sciences of the United States of America*. 105(49): 19282–19287, 2008.
103. M. Cabeen, C. Jacobs-Wagner. Bacterial cell shape. *Nature Reviews Microbiology* 3(8): 601–610, 2005.
104. D. Bonazzi, J. Julien, M. Romao, R. Seddiki, M. Piel, A. Boudaoud, N. Minc. Symmetry Breaking in Spore Germination Relies on an Interplay between Polar Cap Stability and Spore Wall Mechanics. *Developmental Cell* 28(5): 534–546, 2014.
105. V. Davì, N. Minc. Mechanics and morphogenesis of fission yeast cells. *Current Opinion in Microbiology* 28(C):36–45, 2015.
106. N. Goehring, S. Grill. Cell polarity: mechanochemical patterning. *Trends in Cell Biology* 23(2): 72–80, 2013.
107. A. Diz-Muñoz, D. Fletcher, O. Weiner. Use the force: membrane tension as an organizer of cell shape and motility. *Trends in Cell Biology* 23(2): 47–53, 2013.
108. R.M. Neve, K. Chin, J. Fridlyand, J. Yeh, F.L. Baehner, T. Fevr, L. Clark, N. Bayani, J-P Coppe, F. Tong, T. Speed, P.T. Spellman, S. DeVries, A. Lapuk, N.J. Wang, W-L Kuo, J.L. Stilwell, D. Pinkel, D.G. Abertson, F.M. Waldman, F. McCorck, R.B. Dickson, M.D. Johnson, M. Lippman, S. Ethier, A. Gazdar, J.W. Gray. A collection of breast cancer cell lines for the study of functionally distinct cancer subtypes. *Cancer Cell* 10(6): 515-527, 2006.
109. C.M. Perou, T. Sørlie, M.B. Eisen, M. van de Rijn, S.S. Jeffrey, C.A. Rees, J.R. Pollack, D.T. Ross, H. Johnsen, L.A. Akslen, Ø. Fluge, A. Pergamenschikov, C. Williams, S.X. Zhu, P.E. Lønning, A-L Børresen-Dale, P.O. Brown, D. Botstein. Molecular portraits of human breast tumours. *Nature* 406: 747-752, 2000.
110. J.J.F. Sleebom, H.E. Amirabadi, P. Nair, C.M. Sahlgren, J.M.J. den Toonder. Metastasis in context: modeling the tumor microenvironment with cancer-on-a-chip approaches. *Dis Modl Mech* 11(3): dmm033100, 2018.
111. S. Valastyan, R.A. Weinberg. Tumor metastasis: molecular insights and evolving paradigms. *Cell* 147(2): 275-292, 2011.
112. G.P. Gupta, J. Massagué. Cancer metastasis: building a framework. *Cell* 127(4): 679-695, 2006.

113. C.P. Heisenberg, Y. Bellaïche. Forces in tissue morphogenesis and patterning. *Cell* 153(5): 948-962, 2013.
114. M. Lintz, A. Muñoz, C.A. Reinhart-King. The mechanics of single cell and collective migration of tumor cells. *J Biomech Eng* 139(2): 0210051-0210059, 2017.
115. Q. Liu, Q. Luo, Y. Ju, G. Song. Role of the mechanical microenvironment in cancer development and progression. *Cancer Biol Med.* 17(2): 282-292, 2020.
116. E.K. Paluch, C.M. Nelson, N. Biais, B. Fabry, J. Moeller, B.L. Pruitt, C. Wollnik, G. Kudryasheva, F. Rehfeldt, W. Federle. Mechanotransduction: use the force(s). *BMC Biol* 13: 47, 2015.
117. V.M. Weaver. Cell and tissue mechanics: the new cell biology frontier. *Mol Biol Cell* 28(14): 1815-18, 2017.
118. E. Jonietz. Mechanics: the forces of cancer. *Nature* 291: S56-S57, 2012.
119. M.J. Paszek, N. Zahir, K.R. Johnson, J.N. Lakins, G.I. Rozenburg, A. Gefen, C.A. Reinhart-King, S.S. Margulies, M. Dembo, D. Boettiger, D.A. Hammer, V.M. Weaver. Tensional homeostasis and the malignant phenotype. *Cancer Cell* 8(3): 241-254, 2005.
120. V. Swaminathan, K. Myhreye, E.T. O'Brien, A. Berchuck, G.C. Blobe, R. Superfine. Mechanical stiffness grades metastatic potential in patient tumor cells and in cancer cell lines. *Cancer Res* 71(15): 5075-80, 2011.
121. Y.L. Han, A.F. Pegoraro, H. Li, K. Li, Y. Yuan, G. Xu, Z. Gu, J. Sun, Y. Hao, S.K. Gupta, Y. Li, W. Tang, H. Kang, L. Teng, J.J. Fredberg, M. Guo. Cell swelling, softening and invasion in a three-dimensional breast cancer model. *Nature Physics* 16: 101-108, 2020.
122. T.M. Koch, S. Munster, N. Bonakdar, J.P. Butler, B. Fabry. 3D traction forces in cancer cell invasion. *PLOS ONE* (7)3: e33476, 2012.
123. O. Campàs, T. Mammoto, S. Hasso, R.A. Sperling, D. O'Connell, A.G. Bischof, R. Maas, D.A. Weitz, L. Mahadevan, D.E. Ingber. Quantifying cell-generated mechanical forces within living embryonic tissues. *Nat Methods* 11(2): 183-9, 2014.
124. F. Serwane, A. Mongera, P. Rowghanian, D.A. Kealhofer, A.A. Lucio, Z.M. Hockenbery, O. Campàs. *In vivo* quantification of spatially varying mechanical properties in developing tissues. *Nat Methods* 14(2): 181-186, 2017.
125. A.A. Lucio, A. Mongera, E. Shelton, R. Chen, A.M. Doyle, O. Campàs. Spatiotemporal variation of endogenous cell-generated stresses within 3D multicellular spheroids. *Sci Rep* 7(1): 12022, 2017.

126. E. Mohagheghian, J. Luo, J. Chen, G. Chaudhary, J. Chen, J. Sun, R.H. Ewoldt, N. Wang. Quantifying compressive forces between living cell layers and within tissues using elastic round microgels. *Nature Communications* 9: 1878, 2018.
127. W. Lee, N. Kalashnikov, S. Mok, R. Halaoui, E. Kuzmin, A.J. Putnam, S. Takayama, M. Park, L. McCaffrey, R. Zhao, R.L. Leask, C. Moraes. Dispersible hydrogel force sensors reveal patterns of solid mechanical stress in multicellular spheroid cultures. *Nat Comm* 10: 144, 2019.
128. M.E. Dolega, M. Delarue, F. Ingremeau, J. Prost, A. Delon, G. Cappello. Cell-like pressure sensors reveal increase of mechanical stress towards the core of multicellular spheroids under compression. *Nat Comm* 8: 14056, 2017.
129. M. Vinci, C. Box, S.A. Eccles. Three-dimensional (3D) tumor spheroid invasion assay. *J Vis Exp* 99:, 52686, 2015.
130. F. Geiger, L.G. Schnitzler, M.S. Brugger, C. Westerhausen, H. Engelke. Directed invasion of cancer cell spheroids inside 3D collagen matrices oriented by microfluidic flow in experiment and simulation. *PLoS ONE* 17(3): e0264571, 2022.
131. A. Mongera, P. Rowghanian, H.J. Gustafson, E. Shelton, D.A. Kealhofer, E.K. Carn, F. Serwane, A.A. Lucio, J. Giammona, O. Campàs. A fluid-to-solid jamming transition underlies vertebrate body axis elongation. *Nature* 561(7723): 401-405, 2018.
132. B. Gross, E. Shelton, C. Gomez, O. Campàs. STRESS, an automated geometrical characterization of deformable particles for *in vivo* measurements of cell and tissue mechanical stresses. *bioRxiv* 2021.03.26.437148, 2021.
133. S. Kim, M. Pochitaloff, G.A. Stooke-Vaughan, O. Campàs. Embryonic tissues as active foams. *Nature Physics* 17: 859-866, 2021.
134. I. Stamenkovic. Extracellular matrix remodelling: the role of matrix metalloproteinases. *J Pathology* 200(4): 448-464, 2003.
135. J.M. Kelm, N.E. Timmins, C.J. Brown, M. Fussenegger, L.K. Nielsen. Method for generation of homogenous multicellular tumor spheroids applicable to a wide variety of cell types. *Biotechnol Bioeng* 83(2): 173-80, 2003.
136. I. Lim, A. Vian, H.L. van de Wouw, R.A. Day, C. Gomez, Y. Liu, A.L. Rheingold, O. Campàs, E.M. Sletten. Fluorous Soluble Cyanine Dyes for Visualizing Perfluorocarbons in Living Systems. *Journal of the American Chemical Society* 142(37): 16072–16081, 2020.
137. T.H. Chun, M. Inoue. 3-D adipocyte differentiation and peri-adipocyte collagen turnover. *Methods Enzymol* 538: 15-34, 2014.

138. K. Hotary, E. Allen, A. Punturieri, I. Yana, S.J. Weiss. Regulation of cell invasion and morphogenesis in a three-dimensional type I collagen matrix by membrane-type matrix metalloproteinases 1, 2, and 3. *J Cell Bio* 149(6): 1309-1323, 2000.
139. N. Otsu. A threshold selection method from gray-level histograms. *IEEE Transactions on Systems, Man and Cybernetics* 9(1): 62-66, 1979.
140. M. Musy, K. Flaherty, J. Raspopovic, A. Robert-Moreno, J.T. Richtsmeier, J. Sharpe. A quantitative method for staging mouse embryos based on limb morphometry. *Development* 145(7): dev154856, 2018.
141. R. Haase, L.A. Royer, P. Steinbach, D. Schmidt, A. Dibrov, U. Schmidt, M. Weigert, N. Maghelli, P. Tomancak, F. Jug, E.W. Myers. CLIJ: GPU-accelerated image processing for everyone. *Nature Methods* 15: 5-6, 2020.
142. S. Van der Walt, J.L. Schönberger, J. Nunez-Iglesias, F. Boulogne, J.D. Warner, N. Yager, E. Gouillart, T. Yu, the scikit-image contributors. scikit-image: image processing in Python. *PeerJ* 2: e453, 2014.
143. F. Pedregosa, A. Varoquaux, V. Michel, B. Thirion, O. Grisel, M. Blondel, P. Prettenhofer, R. Weiss, V. Dubourg, J. Vanderplas, A. Passos, D. Cournapeau, M. Brucher, M. Perrot, E. Duchesnay. Scikit-learn: machine learning in Python. *Journal of Machine Learning Research* 12: 2825-2830, 2011.
144. A. Hagberg, P. Swart, D.S. Chult. Exploring network structure, dynamics, and function using NetworkX. No. LA-UR-08-05495; LA-UR-08-5495. Los Alamos National Lab.(LANL), Los Alamos, NM (United States), 2008.
145. J. Schaber, M. Angel Adrover, E. Eriksson, S. Pelet, E. Petelenz-Kurdziel, D. Klein, F. Posas, M. Goksor, M. Peter, S. Hohmann, and E. Klipp. Biophysical properties of *Saccharomyces cerevisiae* and their relationship with HOG pathway activation. *European Biophysics Journal with Biophysics Letters* 39(11): 1547–1556, 2010.

## Appendix

Table A:

Parameter	Description	Value
$P$	Turgor pressure of budding yeast	$0.6 \pm 0.2$ MPa [145]
$\rho_w$	Density of 1,3- $\beta$ glucans in cell wall	–
$\mu_0$	Apical viscosity of cell wall	–
$m_w$	Mass of 1,3- $\beta$ glucans monomer	–
$\rho_0$	Density of Fks1/2 enzymes in vesicle	–
$k_p$	Extrusion rate of 1,3- $\beta$ glucans monomers	–
$\lambda_x$	Exocytosis length-scale	$0.6 \pm 0.1$ $\mu\text{m}$ [47] $0.45 \pm 0.1$ $\mu\text{m}$ [95]
$\lambda_D$	Endocytosis length-scale	$1.05 \pm 0.18$ $\mu\text{m}$ [95]
$k_x^0$	Apical rate of exocytosis	$0.045$ $\text{s}^{-1}$ [98]
$k_D^0$	Apical rate of endocytosis	$0.02 \pm 0.02$ $\text{s}^{-1}$ [95] $0.027$ $\text{s}^{-1}$ [98]
$k_{off}$	Inactivation rate of Fks1/2	–

Table B:

Strain	Genotype	Source
RJD863	<i>MATa can-1-100 leu2-3-112 his3-11-15 trp1-1 ura3-1 ade2-1 bar1::hisG</i>	Ray Deshaies
CGY003	<i>RJD863 wsc1A::KAN<sup>R</sup></i>	This study
CGY004	<i>RJD863 mid2A::KAN<sup>R</sup></i>	This study
CGY005	<i>RJD863 wsc1A::HIS5 mid2A::KAN<sup>R</sup></i>	This study
CGY011	<i>RJD863 sec3A::SEC3-GFP-HIS5</i>	This study
CGY012	<i>RJD863 sec3A::SEC3-GFP-HIS5 mid2A::KAN<sup>R</sup></i>	This study
CGY013	<i>RJD863 sec3A::SEC3-GFP-HIS5 wsc1A::LEU2<sup>K1</sup></i>	This study
CGY015	<i>RJD863 sec3A::SEC3-GFP-HIS5 spa2A::LEU2<sup>K1</sup></i>	This study
CGY016	<i>RJD863 sec3A::SEC3-GFP-HIS5 spa2A::LEU2<sup>K1</sup> mid2A::KAN<sup>R</sup></i>	This study
CGY017	<i>RJD863 sec3A::SEC3-GFP-HIS5 spa2A::LEU2<sup>K1</sup> wsc1A::URA3<sup>K1</sup></i>	This study